SPECIAL
Air-sea interaction during PISTON-MISOBOB-CAMP2Ex
COLLECTION

The Coupling between Convective Variability and Large-Scale Flow Patterns Observed during PISTON 2018–19

KYLE CHUDLER[a] AND STEVEN A. RUTLEDGE[a]

[a] *Department of Atmospheric Science, Colorado State University, Fort Collins, Colorado*

(Manuscript received 7 October 2020, in final form 27 May 2021)

ABSTRACT: The Propagation of Intraseasonal Oscillations (PISTON) field campaign took place in the waters of the western tropical North Pacific during the late summer and early fall of 2018 and 2019. During both research cruises, the Colorado State University SEA-POL polarimetric C-band weather radar obtained continuous 3D measurements of oceanic precipitation systems. This study provides an overview of the variability in convection observed during the PISTON cruises, and relates this variability to large-scale atmospheric conditions. Using an objective classification algorithm, precipitation features are identified and labeled by their size (isolated, sub-MCS, MCS) and degree of convective organization (nonlinear, linear). It is shown that although large mesoscale convective systems (MCSs) occurred infrequently (present in 13% of radar scans), they contributed a disproportionately large portion (56%) of the total rain volume. Conversely, small isolated features were present in 91% of scans, yet these features contributed just 11% of the total rain volume, with the bulk of the rainfall owing to warm rain production. Convective rain rates and 30-dBZ echo-top heights increased with feature size and degree of organization. MCSs occurred more frequently in periods of low-level southwesterly winds, and when low-level wind shear was enhanced. By compositing radar and sounding data by phases of easterly waves (of which there were several in 2018), troughs are shown to be associated with increased precipitation and a higher relative frequency of MCS feature occurrence, while ridges are shown to be associated with decreased precipitation and a higher relative frequency of isolated convective features.

KEYWORDS: Atmosphere; North Pacific Ocean; Waves; atmospheric; Precipitation; Radars/radar observations; Radiosonde/rawinsonde observations

1. Introduction and background

a. The PISTON field campaign

Convection and precipitating cumulus in the tropics are of fundamental importance to the atmospheric system, with impacts spanning local to global scales. The structure of precipitating systems is known to directly influence the vertical distribution of latent heating (Houze 1997; Cifelli and Rutledge 1998; Schumacher et al. 2007), and the organization of mesoscale convective systems (MCSs) has been shown to impact momentum transport through the troposphere (LeMone 1983; LeMone et al. 1984). During boreal summer, the western North Pacific ''warm pool'' region is characterized by frequent deep convection. This region is influenced by the low-level westerlies and moisture associated with the Asian summer monsoon (itself a major component of the global weather system), as well as numerous westward moving disturbances in the form of easterly waves (Reed and Recker 1971) and tropical cyclones (Ramsay 2017). Also, an important phenomenon in this region is the boreal summer intraseasonal oscillation (BSISO; Wang and Xie 1997; Lee et al. 2013), marked by an envelope of pronounced convection that propagates from the Indian Ocean northeastward into the western North Pacific. The BSISO has important teleconnections to other areas in the tropics and extratropics (Moon et al. 2013; Lee et al. 2017). For these reasons, the western North Pacific is an enticing region to study.

During the late summer and early fall of 2018 and 2019, the Propagation of Intraseasonal Oscillations (PISTON) field campaign took place in western North Pacific Ocean on board the R/V *Thomas G. Thompson* (hereafter referred to as *TGT*) in 2018 and the R/V *Sally Ride* (hereafter referred to as *SR*) in 2019 (Fig. 1). PISTON originally targeted the South China Sea near the west coast of the Philippines, but refusal of an international marine research agreement forced PISTON to relocate to international waters east of the Philippines. Although no well-defined BSISO oscillation materialized over the course of 69 operational days at sea (20 August–8 September and 14 September–12 October 2018, and 5–24 September 2019), a wide variety of interesting weather conditions were observed. Conditions at the ship varied from fair-weather cumulus and calm seas to intense precipitation and disturbed sea states, the latter situation associated with mesoscale convective systems and the outer rainbands of typhoons overrunning the ship locations. An overview of the large-scale conditions encountered during the 2018 cruise is covered in Sobel et al. (2020).

On board the ships were a suite of scientific instruments, acquiring measurements of the ocean and atmosphere. A key instrument was the Colorado State University SEA-POL

Corresponding author: Kyle Chudler, kyle.chudler@colostate.edu

DOI: 10.1175/JCLI-D-20-0785.1

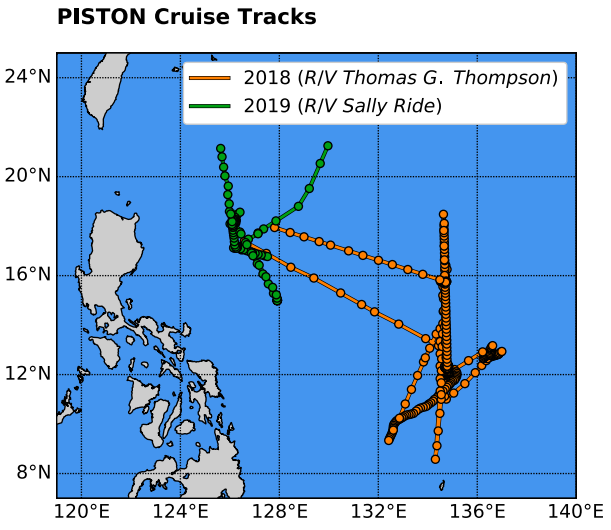

FIG. 1. Ship tracks for the 2018 (20 Aug–8 Sep and 14 Sep–12 Oct 2018) and 2019 (5–24 Sep 2019) PISTON cruises. Outlined circles mark the location of radiosonde launches.

radar, a C-band polarimetric Doppler radar designed for deployment at sea (Rutledge et al. 2019a,b). In addition to providing traditional radar measurements of precipitation intensity and radial velocity, SEA-POL measured a suite of polarimetric variables. The polarimetric variables not only allow for insights into the microphysical properties of storms, but also enable more accurate measurements of rain rate (Thompson et al. 2018). Detailed information on SEA-POL, as well some results from its first deployment at sea [Salinity Processes in the Upper-ocean Regional Study (SPURS-2017)], can be found in Rutledge et al. (2019a,b).

b. Convective morphology

The structure and morphology of precipitating systems in the tropics have important implications on the vertical distributions of heating and momentum transport. Convection in the tropics crosses a wide spectrum of sizes and organizations, from shallow, isolated cells a few kilometers in width (characterized by warm rain processes; Schumacher and Houze 2003), to MCSs hundreds of kilometers wide with organized lines of deep convection and broad areas of stratiform rain (Houze 2014). These systems drive unique latent heating profiles, with shallow convection warming the lower troposphere, deep convection warming the entire troposphere with a peak in the midlevels, and stratiform precipitation warming the upper troposphere while cooling the lower levels (Houze 1989; Schumacher et al. 2007; Tao et al. 2010). Accurate representation of these latent heating profiles in large-scale models has been shown to increase agreement with observations, through generation of a more accurate Walker circulation (Hartmann et al. 1984). With respect to momentum transport, MCSs with linearly organized convective features tend to add momentum in the upper (lower) levels against (along) the direction of propagation (LeMone 1983; LeMone et al. 1984). By characterizing the modes of convection observed during PISTON, this study aims to provide insight which could be used to improve the representation of latent heating and momentum transport in the western North Pacific.

To begin characterizing convective modes, it is desirable to partition radar-observed precipitation into specific categories dictated by their morphology. Rickenbach and Rutledge (1998) manually classified TOGA COARE radar scans into categories by area (MCS and sub-MCS) and organization (linear and nonlinear). Xu and Rutledge (2015, hereafter XR15) improved upon this methodology by developing an automated objective feature classification algorithm which assigned different morphology classifications to each feature within a radar scan, rather than classifying an entire scan under one group, as was done in the manual classification scheme used by Rickenbach and Rutledge (1998). The present study, as discussed in section 2c, incrementally improves the feature identification algorithm by modifying the criteria used for linear and nonlinear classification, as well as introducing an ''isolated'' classification for small convective features.

c. Easterly waves

Easterly waves are a leading mode of convective variability in the tropics (Chang 1970; Burpee 1972; Lau and Lau 1990). Easterly waves are often the precursors of tropical cyclones (Avila and Pasch 1992; Molinari et al. 1997; Dunkerton et al. 2009) and are in fact occasionally referred to in the literature as ''tropical depression–type'' disturbances. In the western North Pacific, easterly waves form from mixed Rossby–gravity waves, which originate along the equator and turn northward as they interact with the confluence zone along the monsoon trough (Dickinson and Molinari 2002; Maloney and Dickinson 2003).

As these waves primarily exist over the open ocean, in situ observations of easterly waves have been sparse, particularly over the west Pacific. Previous studies have relied primarily on satellite (e.g., Kiladis et al. 2006), sounding, or modeling (e.g., Donner et al. 1999) data to describe the 3D variability of convection across easterly waves. Easterly waves were not a focus of study during TOGA COARE (Godfrey et al. 1998) and studies of easterly wave passages during the Kwajalein Experiment (KWAJEX; Sobel et al. 2004; Schumacher et al. 2007; Wang and Zhang 2015) did not examine the vertical structure of convection associated with these waves. Petersen et al. (2003, hereafter P03) used data from the C-band Doppler radar on board the R/V *Ronald H. Brown* to characterize the nature of convection and its vertical structure in different phases of the easterly waves observed during EPIC (East Pacific Investigation of Climate Processes in the Coupled Ocean–Atmosphere System). However, EPIC took place in the eastern Pacific, where the source of easterly waves is different: eastern Pacific easterly waves are tied to African easterly waves, which reintensify over central America (Serra et al. 2008; Whitaker and Maloney 2020), whereas the source of western Pacific easterly waves is less understood, possibly arising due to wave accumulation (a process whereby a zone of confluence, such as that in the western Pacific where trade easterlies meet monsoon westerlies, enhances wave activity; see Maloney and Dickinson 2003; Serra et al. 2008). Fortunately,

during PISTON 2018, several easterly waves passed over the ship (Sobel et al. 2020). Using the method outlined in P03 (described in detail in section 2d) this study identifies easterly wave periods and analyzes the variability in atmospheric conditions and convective morphology across each wave phase.

Overall, the purpose of this study is to provide an overview of precipitation observed by SEA-POL, and to relate the variability in convection to the synoptic patterns documented during each PISTON cruise. Although the SEA-POL radar can only observe precipitation over a relatively small area, broader-scale implications can be inferred by relating this convection and its associated impact on the atmosphere to the synoptic patterns it occurred in. Although this study does not directly address the impact of western Pacific convection on the climate, it does provide a foundation for future work to build upon by linking convective morphologies to different synoptic regimes. An overview of data sources and analysis methods is given in section 2. A brief summary of the large-scale conditions and significant weather events is given in section 3a. Statistics of precipitation feature morphologies and the conditions they occurred in is given in section 3b. An analysis of the easterly waves observed during 2018 is given in sections 3c and 4 summarizes the main findings and conclusions.

2. Data and methodology

a. SEA-POL radar

During the 69 operational days of PISTON over both phases, the SEA-POL radar operated nearly continuously, with only a handful of short (2–3 h) shutdowns needed for maintenance or due to very rough seas (the longest outage was on 24 September 2019, when SEA-POL was shut down for 24 h for repairs). In the 2018 operations, SEA-POL obtained 360° plan position indicator (PPI) volume scans every 15 min, reducing to a 10-min interval in 2019. Multiple elevation sweeps were done in each volume scan, with the exact angles depending on the type and location of echoes present. In general, scanning strategies were chosen that captured the vertical extent of echoes. For example, higher elevation angles were used when storms were closer to the ship. These scanning strategies were designed and programed prior to start of the field campaign. To avoid illuminating the ship's bridge area, a 115° (80°) sector to the aft of SEA-POL was blanked in 2018 (2019; the reason the sector size was smaller in 2019 was due to the smaller ship, *SR*, compared to the *TGT* used in 2018). Nearly 7000 volume scans were collected. Range–height indicator (RHI) scans were also performed both in both phases; however, these scans are not examined in the present study. More detail on SEA-POL and its technical specifications can be found in Rutledge et al. (2019a,b).

The SEA-POL dataset was rigorously quality controlled by the Colorado State University (CSU) Radar Meteorology team prior to analysis. First, nonmeteorological echoes such as sea clutter, side-lobe clutter, second-trip echoes, and other artifacts were removed. Specific differential phase (K_{DP}) calculation and attenuation correction of reflectivity (Z) and differential reflectivity (Z_{DR}) was then performed based on the process outlined in Wang and Chandrasekar (2009). Using the National Center for Atmospheric Research (NCAR) RadX software package (https://ral.ucar.edu/projects/titan/docs/radial_formats/radx.html), radar data were then interpolated on to a 300 km × 300 km Cartesian grid with 15 vertical levels, with grid spacings of 1 km in the horizontal and 0.5 km in the vertical. Radar data were then partitioned into convective and stratiform pixels using the method of Steiner et al. (1995). Finally, rain rate was calculated at each grid point using Z, Z_{DR}, and K_{DP}, based on the method outlined in Thompson et al. (2018).

b. Precipitation features

An improved precipitation feature identification and classification algorithm, based on the method outlined in XR15, is utilized in this study. First, using the gridded radar dataset, precipitation features were identified in each scan by grouping adjacent pixels exceeding a reflectivity threshold (17 dBZ) at a given level (2 km). This threshold was chosen in XR15 to match the minimum detectable reflectivity of the NASA TRMM satellite-based radar, which was also being used in that study. Although TRMM data are not used in the current work, the 17-dBZ threshold was found to capture the majority of features and was therefore retained to facilitate comparisons with the results of XR15. After grouping, the radar echo of each feature was then fit with an ellipse, based on the mass distribution tensor eigenvalues of the raining points (Medioni et al. 2000; Nesbitt et al. 2006). In the event that a feature contained multiple distinct convective elements [as detected by the Steiner et al. (1995) algorithm], each of these convective "subfeatures" was fitted with its own ellipse. This differs from the work of XR15, where convective ellipses were computed to encompass *all* convective points within a feature, regardless of whether these points were connected or not. Fitting separate ellipses to each distinct convective element allows for more accurate classification of the linearity of the convection. For each feature, statistics such as area, mean rain rate, and echo-top height were then calculated.

Once features were identified, a decision tree (Fig. 2) was used to classify features by their morphology. As in XR15, features were labeled as "sub-MCS" or "MCS" based on their overall size. This study also adds the additional size category of "isolated" for features with a maximum horizontal dimension of less than 20 km. Sub-MCS and MCS features were then classified further as "nonlinear" or "linear" based on the length and aspect ratio of the largest convective subfeature contained within the broader echo pattern. Examples of the different types of precipitation features are provided in Fig. 3. For both sub-MCS and MCS features, the aspect ratio of the largest convective feature was required to be less than 0.4 to be classified as linear. Furthermore, for the sub-MCS classification, the largest convective feature also needed to be at least 70% the length of the encompassing main feature. For the linear MCS classification, the largest feature required a length exceeding 50 km. If the largest convective feature within a sub-MCS or MCS did not meet both criteria, the feature was classified as nonlinear. The linearity of isolated features, which

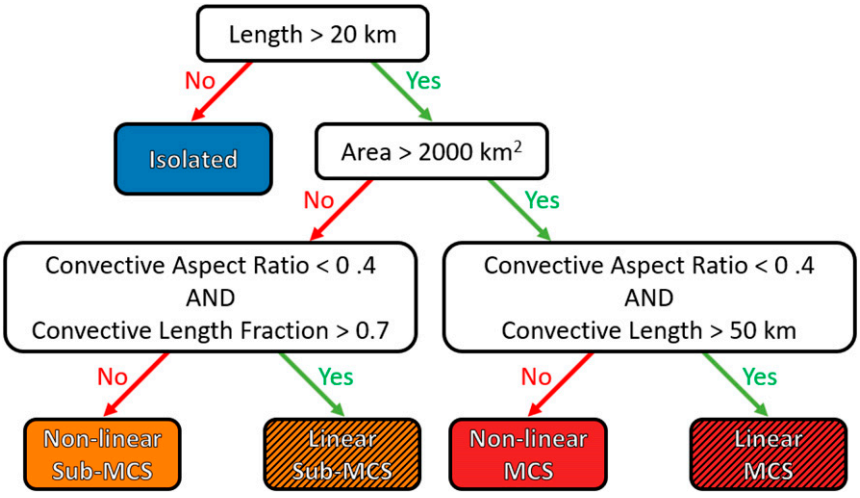

FIG. 2. Decision tree for precipitation feature classification. Convective aspect ratios and lengths are determined by the largest convective feature within the encompassing feature. Convective length fraction is defined as the length of the largest convective feature divided by the length of the whole feature.

are typically short-lived and unorganized, was not considered. The specific thresholds and parameters in the classification decision tree were tuned based on a manual subjective analysis of the algorithm's performance. Sensitivity tests show that, although the specific values of the results presented hereafter do change slightly based on the thresholds and parameters used in classification, the changes are not dramatic and, more importantly, the relative relationship between different morphologies remains the same.

c. *Atmospheric soundings*

Vaisala RS41-SGP radiosondes were launched from the *TGT* and *SR* every 3 h during operational periods of PISTON, making measurements of atmospheric temperature, relative humidity, pressure, and wind speed with a measurement frequency of 1 Hz. Sounding data were then quality controlled as outlined in Ciesielski et al. (2014) and interpolated to 5-hPa intervals. The PISTON sounding operations were overall very successful, with 535 successful launches (375 in 2018 and 160 in 2019). Only a few launches failed to reach the tropopause (balloons launched into moderate or heavy rain would occasionally get stuck or pop around the melting layer, likely due to ice accretion).

d. *Easterly wave detection*

Following methodology of previous studies (e.g., Reed and Recker 1971; Burpee 1974; Burpee 1975; Thompson et al. 1979; P03), 700-hPa meridional wind (v) speed/direction was used to diagnose easterly wave phases in the PISTON 2018 sounding data. No easterly waves were observed in 2019 [the weather was primarily influenced by a monsoon depression; see section 3a(2)], and therefore the 2019 dataset is excluded from the easterly wave analysis. To isolate the easterly wave signal, a Butterworth bandpass filter was applied to the 5-hPa interpolated sounding data to emphasize signals with periods of 3–7 days. Based on the magnitude/sign of v, each sounding profile was then defined as being in one of four wave phases: ridge, northerly, trough, or southerly. Ridges and troughs were defined as times when the magnitude of v was less than $2\,\mathrm{m\,s^{-1}}$, with ridges being in a transition from northerly to southerly wind, and vice versa for troughs. Periods when v was less than $-2\,\mathrm{m\,s^{-1}}$ were labeled as northerly, and periods when v was greater than $2\,\mathrm{m\,s^{-1}}$ were labeled as southerly. Put more succinctly:

- Ridge: transition from southerly to northerly, $|v| < 2\,\mathrm{m\,s^{-1}}$
- Northerly: $v < -2\,\mathrm{m\,s^{-1}}$
- Trough: transition from northerly to southerly, $|v| < 2\,\mathrm{m\,s^{-1}}$
- Southerly: $v > 2\,\mathrm{m\,s^{-1}}$

As this method only looks at the local meridional wind direction without context of the larger environment it was occurring in, a baseline assumption is that variation in the meridional wind is primarily due to easterly wave activity. This was largely true for the 2018 cruise (Sobel et al. 2020), with the notable exception of when tropical cyclones passed near the ship. Periods that were significantly impacted by typhoon activity (i.e., when in the ''monsoon tail'' of Jebi; see Sobel et al. 2020) were subjectively identified and removed.

e. *Other data sources*

Tropical cyclone track and intensity data were obtained from the IBTrACS database (Knapp et al. 2010, 2018). Gridded reanalysis of meteorological fields was obtained from the fifth-generation European Centre for Medium-Range Weather Forecasts Reanalysis product (ERA5; Hersbach et al. 2020). Gridded global precipitation estimates from the Integrated Multisatellite Retrievals for GPM (IMERG) version 6 dataset (Tan et al. 2019) are also used in this study. Sea surface temperature was calculated by the National Oceanic and

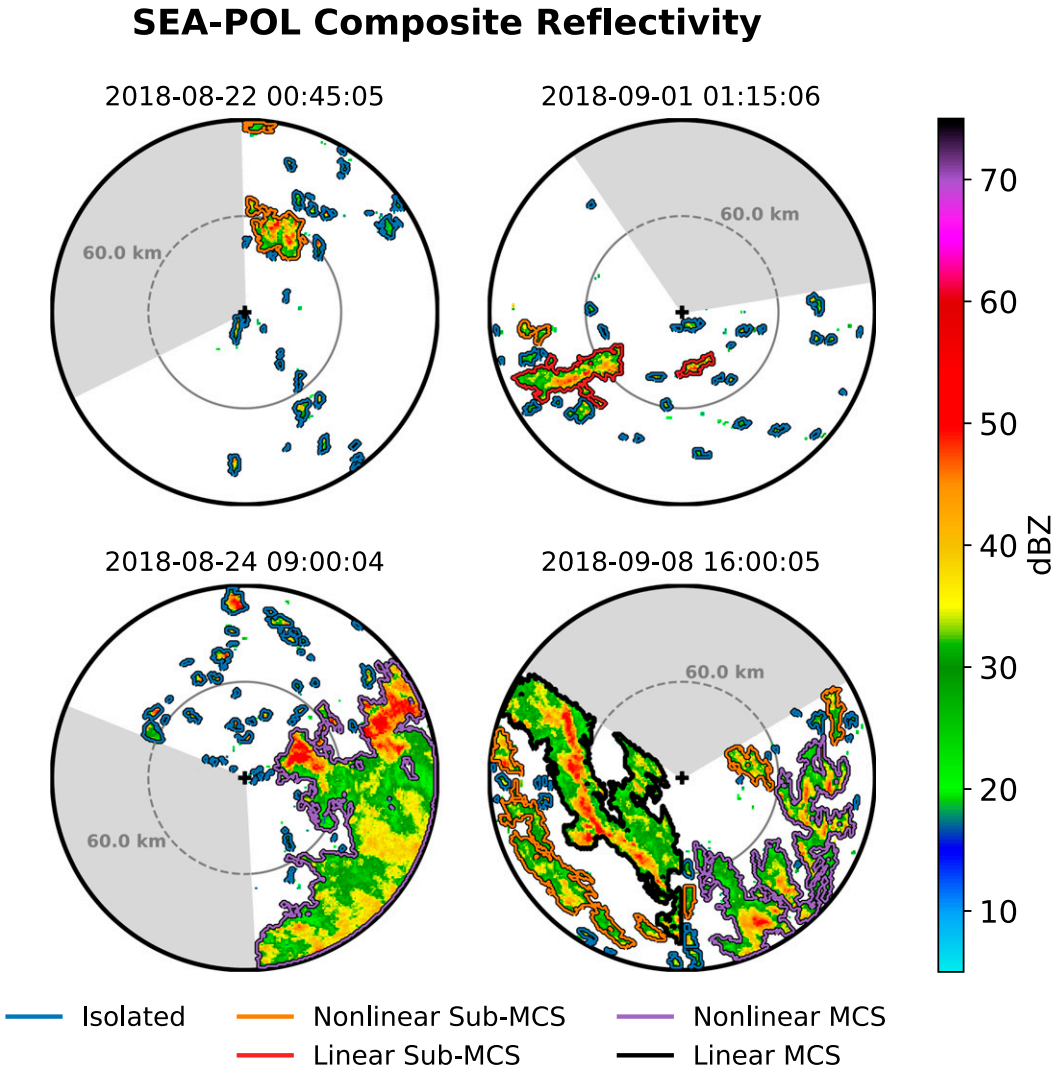

FIG. 3. SEA-POL composite reflectivity images showcasing examples of the different types of precipitation features used in this study. Each feature is outlined with a color corresponding to its feature type, as provided in the legend on the bottom. The gray wedge indicates the portion of SEA-POL's scope, which was blanked in order to avoid radiating the ship's bridge.

Atmospheric Administration Physical Sciences Laboratory (NOAA PSL) using the COARE 3.6 algorithm (Edson et al. 2013; documentation of most recent version available at ftp://ftp.etl.noaa.gov/BLO/Air-Sea/bulkalg/cor3_6/), based on an infrared radiometer and towed thermistor. The COARE algorithm accounts for sharp gradients in temperature on the skin of the ocean surface that cannot be captured by the radiometer/thermistor alone.

3. Results

a. Overview of cruises

Although a well-defined BSISO event did not occur in either the 2018 or 2019 PISTON cruises, both cruises did experience a variety of atmospheric conditions, both large-scale and locally. This section will discuss the large-scale conditions that occurred during each cruise and relate these large-scale patterns to time series of PISTON radiosonde and ship radar measurements.

1) 2018

Sobel et al. (2020) examined the large-scale conditions during the 2018 cruise. The cruise was generally characterized by a background easterly flow, with embedded westward moving disturbances (easterly waves) that propagated over the operations area on the time scale of a few days. This was particularly true in the first leg of the 2018 cruise (late August–early September). In addition to these easterly waves, the cruise was also punctuated by six tropical cyclones, all of which passed to the north of the *TGT* with a

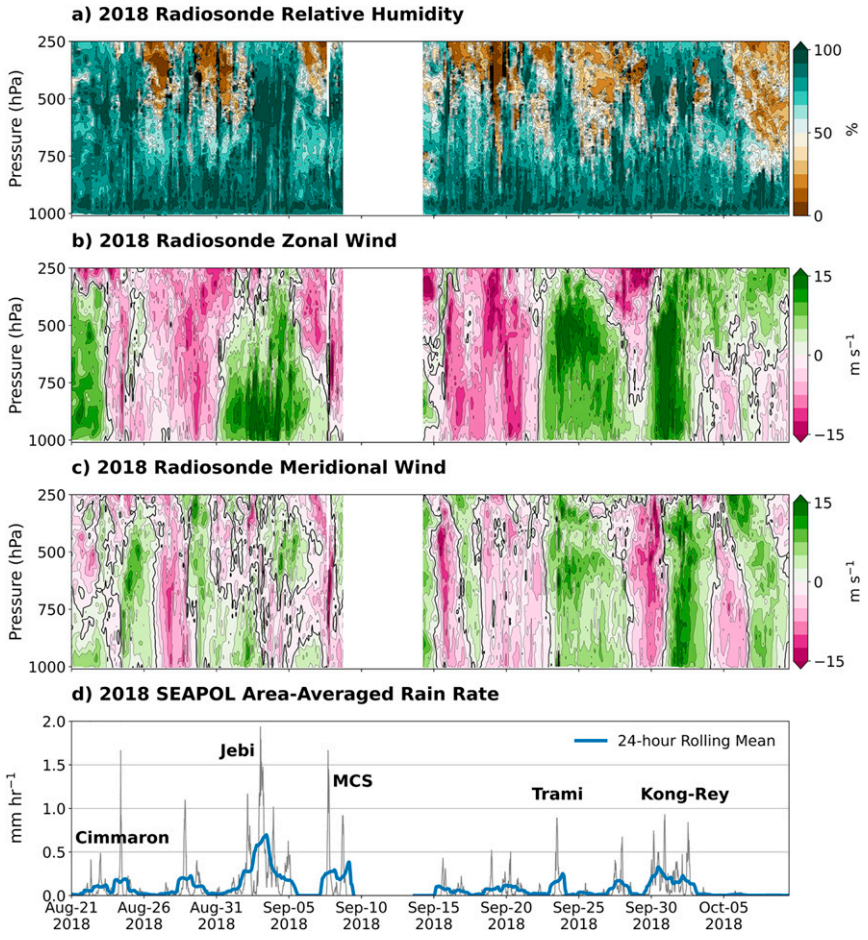

FIG. 4. Time–height time series of (a) relative humidity, (b) zonal wind, and (c) meridional wind, and (d) unconditional area-averaged rain rate as measured by SEA-POL during the 2018 cruise. The thin gray line in (d) is the mean value from every SEA-POL scan, while the thicker blue line is a 24-h rolling mean. Notable events are annotated in (d) around the time they occurred. The blank space in mid-September coincides with when the ship was in port and not taking measurements.

range of intensities. The climatological number of tropical cyclones (TCs) within a 20° × 20° box centered at 15°N, 133°E during the PISTON operations period (20 August–12 October 2018) is 5.9, as calculated from the IBTrACS dataset. During these TC passages, the *TGT* experienced enhanced low-level westerlies, as the monsoon flow to the west expanded eastward and merged with the inflow on the southern flanks of the cyclones. These ''monsoon tails'' (belts of strong southwesterly winds and enhanced precipitation linking the monsoon region to the inflow of the storm) are discussed briefly in Sobel et al. (2020) and are a likely topic of future investigation.

A time–height plot of sounding data is shown in Fig. 4. In mid- to late-August and in early October, periods of 5-day oscillations between northerly and southerly winds can be seen in the meridional wind (Fig. 4c). These signatures mark easterly wave passages, as mentioned previously (also see discussion in section 2d and Fig. 15). Extended periods of low-level westerlies (e.g., 1–5 and 23–27 September) occurred when TCs passed to the north of the TGT. During these TC periods an easterly wave signal (i.e., a 5-day oscillation of meridional winds) is not evident. An intrusion of dry air can be seen in the relative humidity field (Fig. 3a) toward the end of the cruise, starting in the upper levels around 5 October and descending to the middle and lower levels over the next few days. Sobel et al. (2020) attributes this period of subsidence and drying to a suppressed phase intraseasonal oscillation (ISO) that propagated across the study region during this time.

A time series of area-mean rain rate as observed by SEA-POL is shown in Fig. 4d. Significant events are annotated. The highest mean rain rates generally occurred with the passage of rainbands associated with the TCs. The exception to this was an MCS that was not associated with a TC that impacted the ship on the night of 7 September. The highest area-mean rain-rate values were generally in the 1–2 mm h^{-1} range, which is similar to what was seen by the C-band radars in TOGA

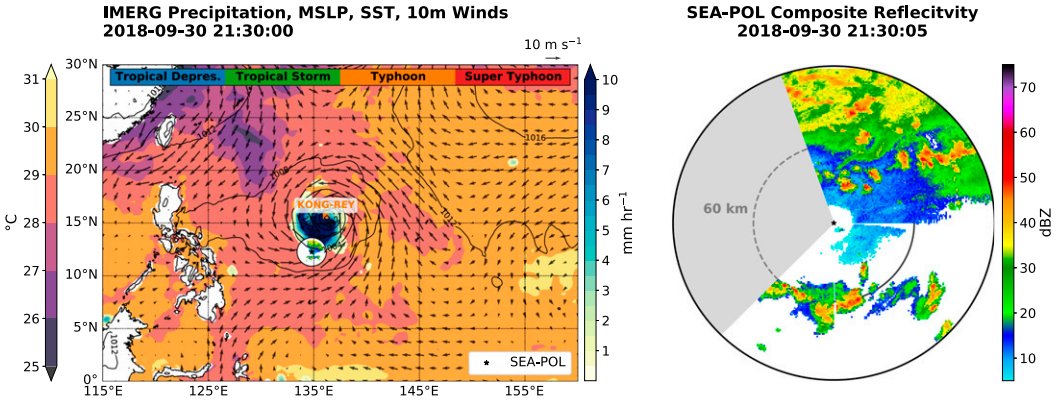

FIG. 5. (left) IMERG precipitation (green–blue fill), ERA5 SSTs (purple–orange fill), 10-m wind speed, and MSLP (black contours) and (right) SEA-POL reflectivity at the same time. The location of Typhoon Kong-Rey is noted by the orange marker. The gray wedge indicates the portion of SEA-POL's scope that was blanked in order to avoid radiating the ship's bridge. This image is part of a movie covering the entire cruise, available at http://radarmet.atmos.colostate.edu/piston/.

COARE (Rickenbach and Rutledge 1998) and DYNAMO (XR15). In late September to early October, Typhoon Kong-Rey passed within 400 km of the ship. A snapshot of this event from 2130 UTC 30 September at is shown in Fig. 5. This passage is marked by a period of strong westerlies and increased rain rates (Fig. 4d). At the time of Kong-Rey's closest proximity to the *TGT,* wind gusts of 15 m s^{-1} and significant wave heights of up to 4.5 m were observed at the ship. After the passage of Kong-Rey, precipitation was almost completely absent. This period coincided with the suppressed phase ISO discussed earlier.

Figure 4d shows some evidence of a rainfall peak approximately every 5 days. It is tempting to link this pattern to easterly waves, which occur on similar time scales. However, because the signal in Fig. 4d is conflated with tropical cyclone precipitation, the apparent pattern in rain rate cannot be strictly tied to easterly wave processes.

2) 2019

Sounding time–height and SEA-POL rain-rate time series plots for 2019 are given in Fig. 6. Unlike the 2018 cruise, which featured numerous easterly waves and tropical cyclones, the "weather" during the 2019 cruise was mainly influenced by a single system. A large monsoon depression (e.g., Beattie and Elsberry 2012), labeled as Invest 95W by the Joint Typhoon Warning Center (JTWC), meandered about the west Pacific for the duration of the *SR* cruise. From 10 September onward, the variability in sounding winds (Figs. 6b,c) is primarily tied to the location of 95W and where within its broad cyclonic circulation the *SR* was situated. The monsoon depression initially formed to the southeast of the operations area (Fig. 7), placing the ship in the northwest quadrant under northeasterly winds. 95W then moved to the north of the ship, fluctuating in degree of organization and intensity. On 19 September, 95W finally consolidated and strengthened into Tropical Storm Tapah, as it moved to the northwest of the ship, placing the *SR* in a region of strong southwesterly inflow. At this point, another monsoon tail formed (Fig. 8), as was common in the 2018 cruise. Fluctuations in rain rate recorded by SEA-POL (Fig. 6d) after 10 September can primarily be tied to fluctuations in the strength of 95W/Tapah, with MCSs embedded within the larger-scale tropical storm rainbands moving across the radar observational domain.

b. Precipitation features

A time series of precipitation feature count, mean 30-dB*Z* echo-top heights, and mean rain volume is shown in Fig. 9. Linear and nonlinear features are grouped together for this analysis. For both the 2018 and 2019 cruise, small isolated features occurred most frequently, MCSs occurred the least frequently, and sub-MCSs fell approximately in the middle. Isolated features were present almost throughout the duration of both cruises. Note that for this feature count, which is calculated as a count per 3-h window, a single feature may be counted multiple times if it persists for multiple scans within the 3-h window. However, this multiple-counting effect is expected to be approximately equal for all morphologies, so it is still a valid metric to use.

Examining the 30-dB*Z* echo-top heights (Figs. 9b,e), isolated features generally had the lowest heights, MCSs had the highest, and again sub-MCS features fell in the middle. It is interesting to note that there was not much fluctuation in mean 30-dB*Z* echo-top height for isolated and sub-MCS over time for either cruise (MCSs were infrequent, so conclusions about their temporal consistency are not made here). A possible exception to this is near the end (6 October onward) of the 2018 cruise, where the mean 30-dB*Z* height of isolated features appears to decrease by 1–2 km. This coincides with the dry-air intrusion seen in Fig. 4a, as well as the arrival of the suppressed phase ISO noted by Sobel et al. (2020), both of which would have acted to reduce echo intensity. Also note that the 30-dB*Z* echo-top height of isolated features rarely gets above the freezing level. This suggests that ice-based processes were infrequent in these echoes; instead, these features were associated

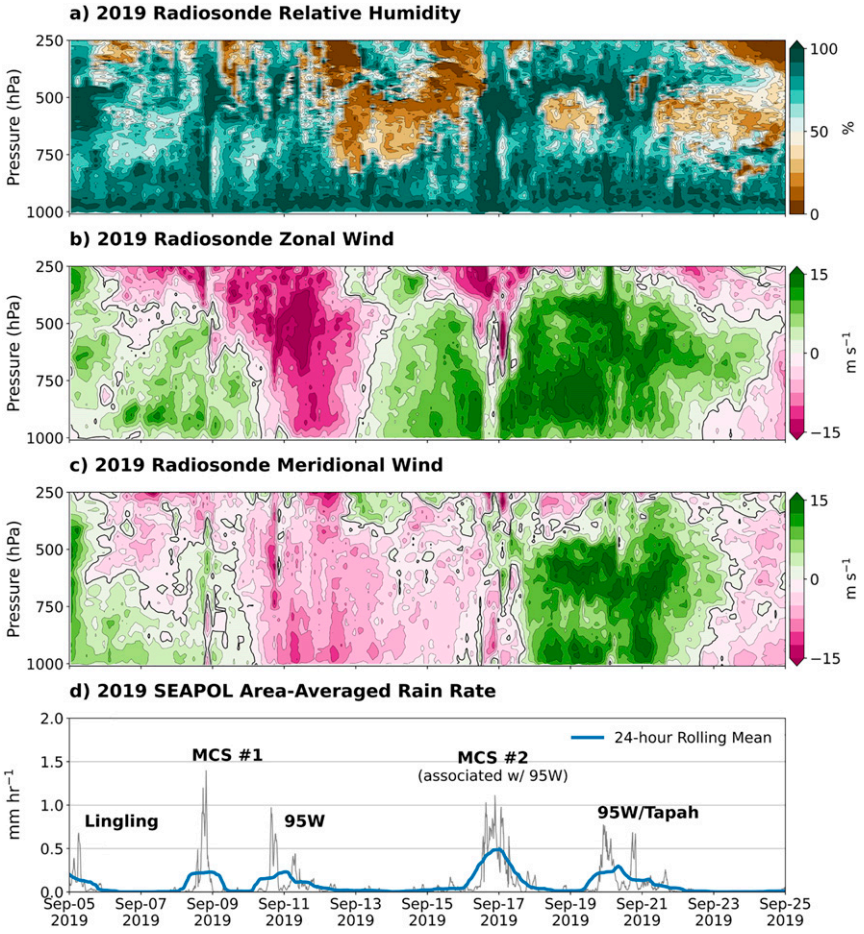

FIG. 6. As in Fig. 4, but for the 2019 PISTON cruise. Note that the time scale on the x axis is different than in Fig. 4.

with warm rain processes. However, it is important to consider that this plot includes features at all stages in their life cycles, not just at their maximum intensity. It is probable that the mean echo height of isolated features would be higher if features were only considered at their maximum intensity. This is point is touched on in a later section.

Rain volume (defined as mean rain rate of a feature multiplied by its area) is dominated by MCSs, for both cruises

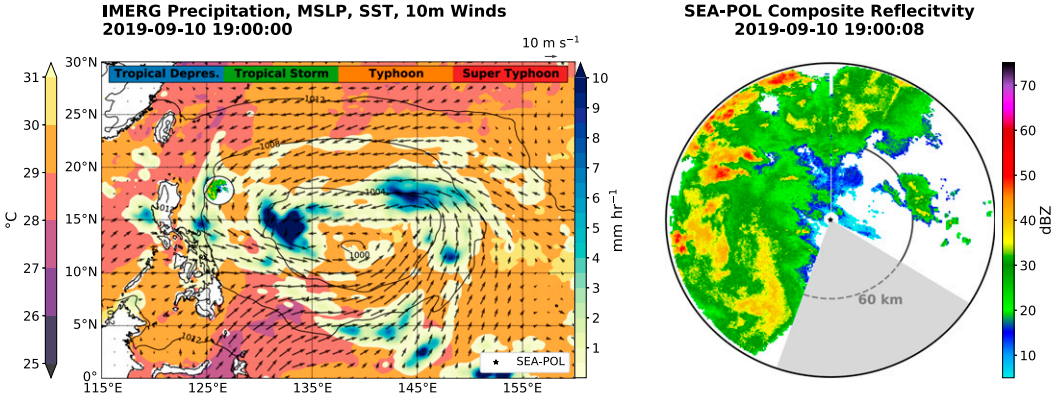

FIG. 7. As in Fig. 5, but during the 2019 cruise. The large monsoon gyre 95W can been seen centered around 12.5°N, 137°E.

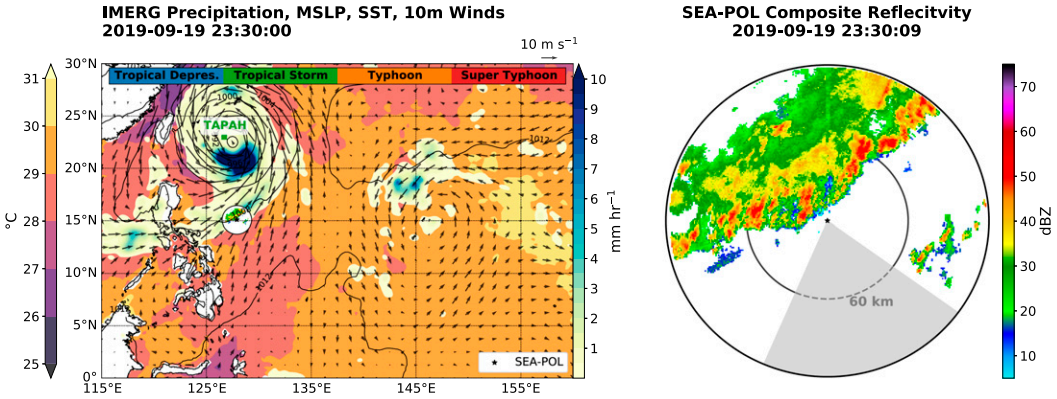

FIG. 8. As in Fig. 5, but depicting Tropical Storm Tapah and its monsoon tail, which was impacting the ship at the time.

(Figs. 9c,f). Individual peaks in the rain volume time series match well with the peaks in area-mean rain rate in Figs. 4d and 6d, as typhoon rainbands contained large MCSs with strong embedded convection. Note that although the scale of the *y* axes on Figs. 9c and 9f is too large to show it, isolated features also contribute a relatively small but consistent rain volume of around 100 km^2 mm h^{-1}.

Statistics of the different feature morphologies are plotted in Fig. 10. The ubiquitous nature of isolated cells is once again apparent, with isolated features identified in 91% of the SEA-POL scans (Fig. 10a). With increasing size (isolated to sub-MCS to MCS) and organization (nonlinear to linear), the morphology frequency decreases. A different pattern is apparent for rain volume (Fig. 10b). Despite only being present in 13% of SEA-POL scans, MCSs (linear and nonlinear combined) contributed 56% of the total rain volume. In addition to their larger area, Figs. 10c and 10d also show that convective cells within MCSs tended to have higher rain rates and higher 30-dB*Z* echo-top heights, both consistent with increased intensity. For the case of a nonlinear MCS especially, we speculate that this increased cell intensity may be due to cells being less susceptible to entrainment as they are embedded within stratiform areas. Interestingly, mean convective rain rate and 30-dB*Z* echo-top heights of convective cells with linear configuration tended to be enhanced relative to their nonlinear counterparts. The reason for this is unclear and is not examined in this study. Overall, the large raining area of MCSs, combined with their intense embedded convection, allowed for MCSs to dominate the rain volume contribution, despite their infrequent occurrence.

Isolated features on the other hand contribute 11% of the rain volume, despite being present 91% of the time. However, 11% is a nonnegligible portion of the total rain. It should also be noted that this analysis considers features at all stages in their life cycle, not just at their maximum intensity. Weak isolated features that are just forming or nearly dissipated are included in this calculation and will bring down the mean convective rain rates and 30-dB*Z* echo-top heights. This effect can clearly be seen in the 30-dB*Z* echo-top height boxplot for isolated features, where the entire lower quartile of the data consists of features with reflectivity < 30 dB*Z* (i.e., a 30-dB*Z* echo-top height of 0 km). The impact of this can also be seen in the skewedness of the convective rain-rate distribution, which has a long upper tail. This is likely and artifact of the relatively short lifespan of these isolated cells, and the fact that their peak intensity is rather brief. The ''forming'' and ''dissipating'' stages of these cells' life cycles make up a large portion of their existence, and therefore SEA-POL was more likely to sample cells in one of these weaker stages at any given time. However, when isolated features were sampled at near maximum intensity, they had convective rain rates on par with that of sub-MCSs and MCSs (although again these rain rates were relatively short in duration). While MCSs at various points in their life cycles are also included in this analysis, even the weakest MCSs likely had some embedded convection remaining in it, so they are not as susceptible to this factor. The 11% rain contribution from isolated cells is in close agreement with Rickenbach and Rutledge (1998), who found that isolated convective cells accounted for 12% of the total rainfall observed by the two TOGA COARE ship radars.

c. *Precipitation features versus environmental conditions*

In this section we examine the relationship between precipitation feature morphology and environmental conditions. First, the influence of active monsoon conditions (defined as periods with strong southwesterly winds) on feature morphology is examined. Figure 11 shows the distribution of convective morphologies by wind direction. Here, a wind vector was associated with each feature based on the mean low-level (1000–850 hPa) wind recorded by the sounding launched nearest to the time of the feature's occurrence. A feature was labeled as having occurred in a southwesterly regime if the magnitude of the southwesterly component of the wind vector associated with that feature was greater than 3 m s^{-1}. Because of the unequal sampling of southwesterly and nonsouthwesterly regimes, the following resampling method was preformed to insure equal representation. Each SEA-POL scan was first labeled as occurring in a southwesterly or nonsouthwesterly regime, following the

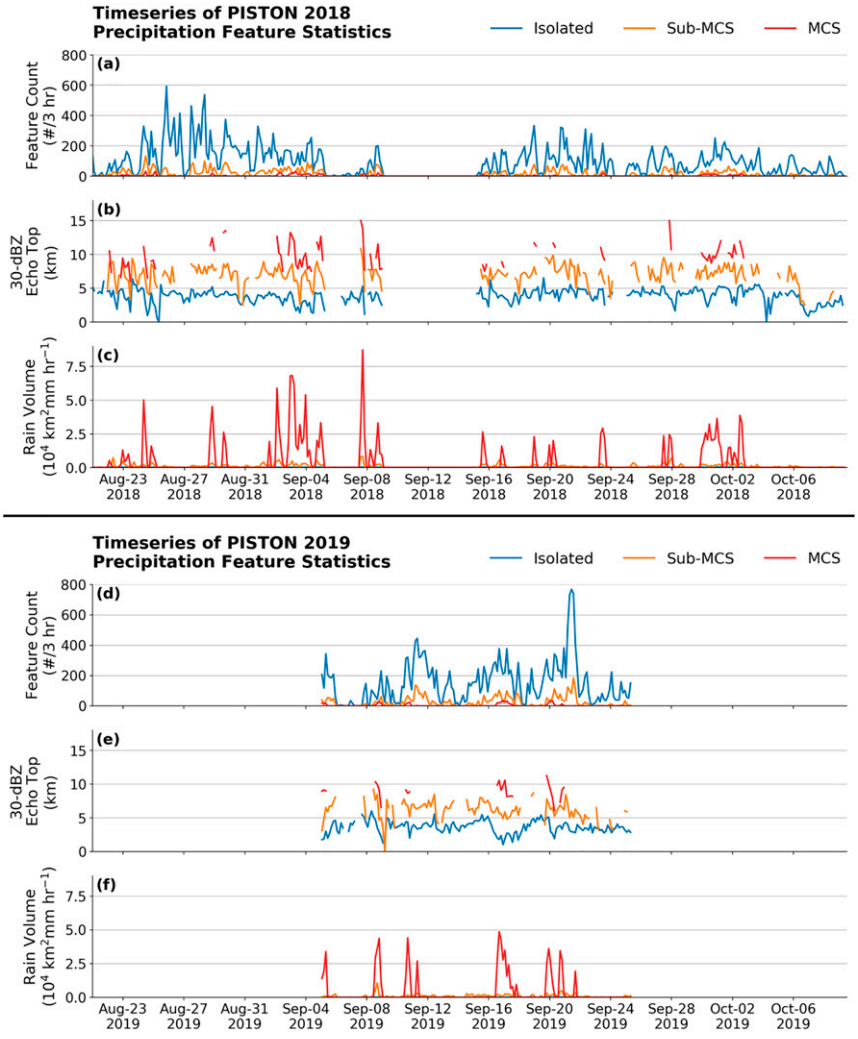

FIG. 9. (a),(d) Time series of precipitation feature count, (b),(e) 30-dBZ echo-top height, and (c),(f) rain volume for the PISTON (a)–(c) 2018 and (d)–(f) 2019 cruises. Data were binned every 3 h. Feature count shows the total number of features that occurred in each 3-h bin, while 30-dBZ echo-top height and rain volume show the mean value for all features of a given type in each 3-h bin.

method above. Then 1000 radar scans were chosen at random from each regime, and the precipitation features were tallied from these scans. Comparisons between other wind regimes were also performed, but showed little to no difference in feature frequency. Because of this, and because the southwest monsoon flow is of particular importance in this region, this study will focus only on the difference between designated southwesterly and nonsouthwesterly regimes.

Figure 11 shows that approximately equal numbers of isolated and sub-MCS features occurred in southwesterly and nonsouthwesterly regimes. MCSs, however, were far more common in the southwesterly regime. This agrees with the results of Xu and Rutledge (2018) and Chudler et al. (2020) showing that larger features were more frequently present over the South China Sea during periods of strong southwesterly flow. These studies attributed this increase to the enhanced midlevel moisture, surface hear/moisture fluxes, and wind shear present during periods of strong southwesterly flow. Although the current study is examining a different region (east of the Philippines rather than west), it seems reasonable that the same explanation applies here. However, the focus of Xu and Rutledge (2018) and Chudler et al. (2020) was on the BSISO (active BSISO phases are associated with southwesterly winds), and there was no significant BSISO activity during PISTON. Additionally, many of the southwesterly wind regimes during PISTON (specifically during 2018) occurred when a typhoon was passing to the north of the ship, and the increase in MCSs may have been induced by the passing typhoons, especially their outer rainbands. As discussed previously, the rain on the southern flank of these typhoons were often enhanced with a belt of southwesterlies (a ‘‘monsoon

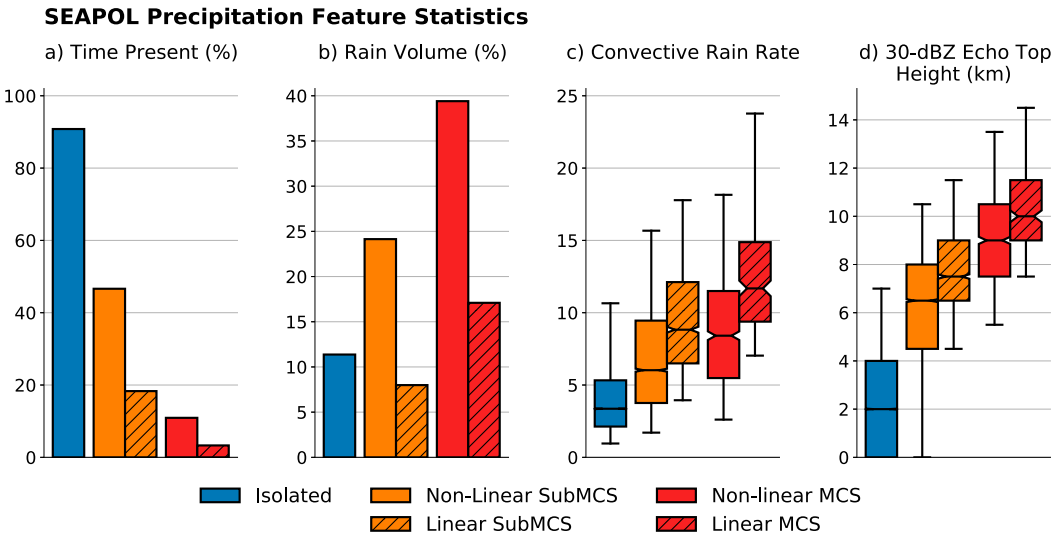

FIG. 10. SEA-POL precipitation feature (a) occurrence frequency, (b) rain volume fraction, (c) convective rain-rate distribution, and (d) 30-dBZ echo-top height distribution from both PISTON cruises. Boxplot whiskers represent the 5th and 95th percentiles of the data. Notches around the boxplot median values represent the confidence interval around the median, as calculated using a Gaussian-based asymptotic approximation.

tail'') connecting the typhoon to the core monsoon region, which could enhance precipitation and possibly MCS activity. Regardless of the exact mechanism, a consistent correlation between enhanced southwest monsoon flow and MCS frequency is noted between this current study, Xu and Rutledge (2018), and Chudler et al. (2020).

Figure 12 shows the distribution of low-level (1000–850 hPa) wind shear (Fig. 12a), convective available potential energy (CAPE; Fig. 12b), and sea surface temperature (SST; Fig. 12c) associated with the five convective morphologies. Although the distributions in the figure are similar and overlap to a degree, there are statistically significant differences in the median values (as indicated by the notches in the boxplots; see figure description) for different morphologies, which will be discussed here. MCSs tended to occur in higher wind shear regimes than isolated or sub-MCSs. Increased low-level wind shear has been shown to lead to an increase in convective organization, which may have aided the formation of MCSs (Thorpe et al. 1982; LeMone et al. 1998; Lang et al. 2007). However, mesoscale flow features within MCSs can also act to increase low-level shear (i.e., a descending rear inflow jet). Therefore, it cannot be ruled out that the observed increase in shear may be due to processes within MCSs themselves, rather than changes background environmental conditions. An example of this is provided in Fig. 13, which shows a vertical cross section of an MCS observed by SEA-POL during PISTON 2019. Here, a descending rear inflow jet can be seen underlying a region of front-to-rear outflow, leading to strong vertical wind shear. Unlike wind shear, CAPE is notably lower for MCSs than for other morphologies. This could be a result of soundings that were launched into MCSs, or soundings that experienced surface air that had been modified by nearby MCSs. For example, these MCSs likely produced substantial cold pools, evaporative cooling below their stratiform components, and reduced solar heating of the surface due to cloud shading. Each of these processes would serve to reduce the low-level temperature, which would in turn reduce surface-based CAPE. This relationship can be seen in Fig. 14. In addition to CAPE being lower near MCSs, Fig. 14 also shows that lower surface to 1.5-km mean temperatures correlate with decreasing instability. Furthermore, convective air motions within the MCSs themselves may reduce instability by adjusting the local temperature profile toward moist adiabatic (i.e., the convective adjustment process). This is all to say that there are several reasons to expect lower instability

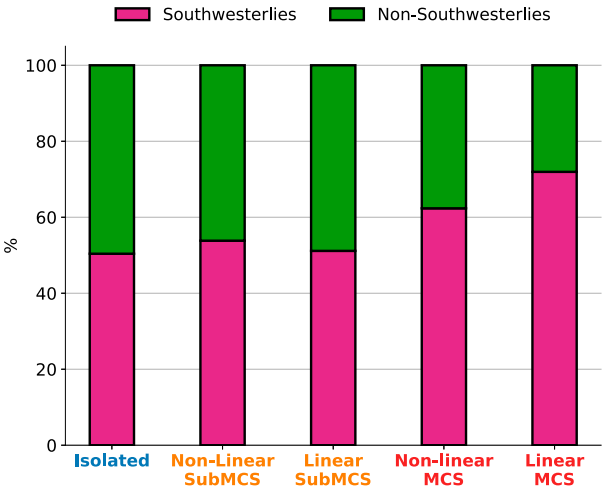

FIG. 11. Distribution of wind directions at time of occurrence for different feature morphologies. Southwesterlies and nonsouthwesterlies were sampled equally using the random-sampling method, described in section 3c.

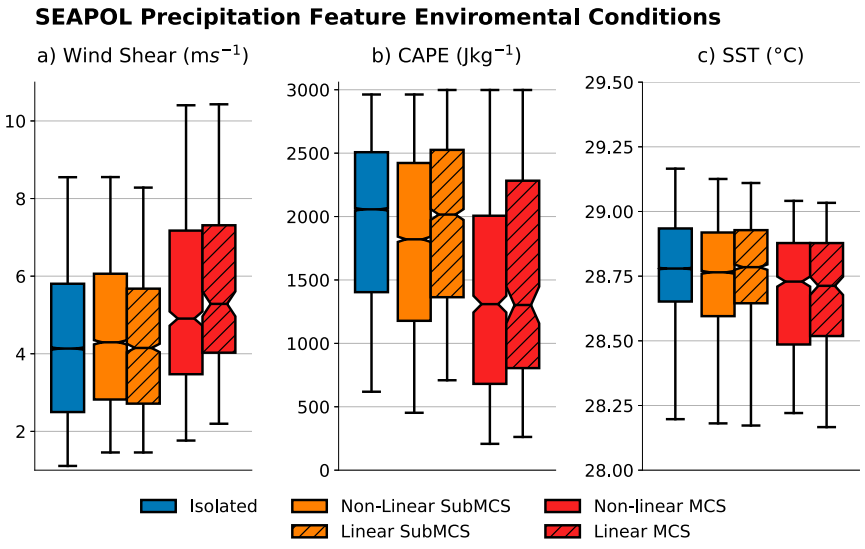

FIG. 12. (a) 1000–850-hPa wind shear, (b) convective available potential energy (CAPE), and (c) SST statistics for different feature morphologies. Wind shear and CAPE values are derived from atmospheric soundings. SST was calculated based on measurements from an infrared radiometer and a towed thermistor.

in and around MCSs, as seen in Fig. 12. Similarly, the SSTs associated with MCSs are slightly lower than other morphologies, likely due to extensive cloud shielding and reduced solar insolation. For sub-MCSs, linear systems tended to form in higher-shear environments that nonlinear systems. This agrees with previous studies that highlighted the importance of low-level shear in generating organized convective lines (Houze and Cheng 1977; Rotunno et al. 1988; LeMone et al. 1998; Weisman et al. 1988; Weisman and Rotunno 2004; Liu and Zipser 2013).

d. *Easterly waves*

This section will examine the how environmental conditions and precipitation feature statistics varied over different easterly wave phases observed during the 2018 cruise. Details on the methodology used for wave phase detection can be found in section 2d.

Figure 15 shows a time–height plot of meridional wind (v), both with and without a 3–7-day bandpass filter applied (Figs. 15a and 15b, respectively). A time series plot of 700-hPa wind, with easterly wave phases marked, is also provided in Fig. 15c. As expected, the bandpass filter effectively culls out variation in the meridional wind on the time scale of easterly waves. Oscillations in the meridional wind on a time scale of 3–5 days are clearly seen in the filtered plot. Wave phases are also marked in the middle of the plot, as labeled by the automated detection algorithm discussed in section 2d. Northerly (southerly) phases correspond with a filtered 700-hPa wind of less than $-2\,\mathrm{m\,s^{-1}}$ (greater than $2\,\mathrm{m\,s^{-1}}$), and toughs and ridges fall in between. The 18

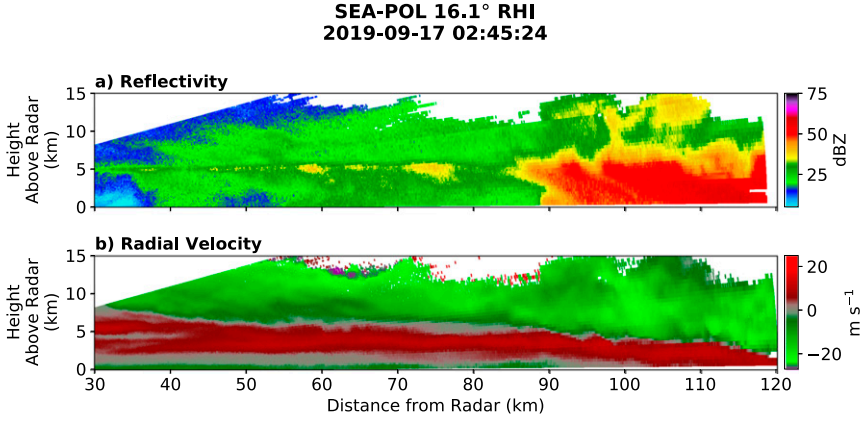

FIG. 13. Vertical cross section of (a) radar reflectivity and (b) radial velocity from a MCS observed by SEA-POL during the 2019 cruise.

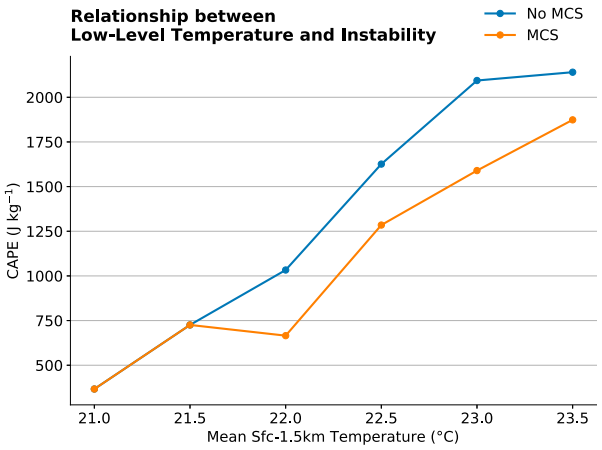

FIG. 14. Mean convective available potential energy (CAPE) for different mean boundary layer height temperatures for times where an MCS was present (orange line) and where no MCS was present (blue line).

September–4 October period was not considered in this analysis, as that period was significantly influenced by the passage of Typhoon Trami and Super Typhoon Kong-Rey. Overall, only two full wave events were captured, in addition to two ''partial'' wave events. However, the ship made a run north just before port call (to make oceanographic transects ahead of a typhoon), and in doing so moved out of the wave, so the other phases were not captured. In total, four northerly periods, four troughs, two ridges, and five southerly periods were detected. Given this relatively small sample size, the following discussion may not necessarily be representative of all easterly waves in this region, and caution should be exercised in generalizing results. However, the uniqueness of these measurements makes this analysis valuable. The wave phases as labeled by the automated detection algorithm were subjectively verified through manual inspection of ERA5 wind and pressure fields. Although the ship did move around during the field campaign, the spatial extent of the movement during easterly wave passages was small compared to the size of the waves themselves, so results should not be significantly impacted.

Radiosonde measurements were composited by wave phase (shown in Fig. 16). The composited meridional wind appears as expected, with a southerly wind signal throughout the column associated with the southerly phase, and northerly wind associated with the northerly phase (Fig. 16b). The zonal wind pattern (Fig. 16a) shows an easterly (westerly) anomaly in the trough (ridge) phase from the surface to about 500 hPa, with some evidence of a reversal in direction above that level. For temperatures (Fig. 16c), southerly (northerly) phases featured warm (cold) anomalies throughout most of the column, with the exception of the surface to 900-hPa level, wherein the anomalies were shifted about 90°, and warm (cold) anomalies were found in the ridge (trough) phase. For relative humidity (Fig. 16d), troughs (ridges) were associated with moist (dry) anomalies throughout the column.

The relations discussed above differ in several ways from the results of P03. Looking at easterly waves in the eastern Pacific, P03 found that u and v were positively correlated. However, in this study, u and v appear to be about 90° out of phase, with v peaking in southerly phases and u peaking in troughs. This is important, as a positive correlation of u and v is needed for barotropic conversion of eddy available potential energy to kinetic energy (Maloney and Dickinson 2003; P03). The fact that the waves observed during PISTON apparently did not feature positively correlated u and v winds (i.e., the waves were not tilted in the horizontal plane) suggests that these waves were drawing their energy from some other process. P03 also noted a westward tilt with height in the waves they analyzed, suggesting the possibility of baroclinic energy conversion (e.g., Lau and Lau 1992; Maloney and Dickinson 2003), but no significant tilt is evident in Fig. 16, so baroclinic contribution to wave growth also appears to be insignificant for the PISTON waves. This leaves diabatic heating as the remaining possible energy source, wherein the latent heat release and rising air within convection leads to generation of eddy kinetic energy. This is further supported by the fact that area-mean rain-rate anomalies maximize in the trough and southerly phases (not shown), which matches the location of positive temperature anomalies in Fig. 16c. Additionally, P03 found that at low levels, warming (cooling) occurred in the northerly (southerly) phase, while this study finds warm (cold) low levels in the ridge (trough) phase. Overall, it is not too shocking that the structure of the PISTON easterly waves differs from those analyzed in P03, as they occurred in different areas of the world (the western and eastern Pacific, respectively), where the sources and energetics differ substantially (Thorncroft and Hoskins 1994a; Thorncroft and Hoskins 1994b; Dickinson and Molinari 2002; Maloney and Dickinson 2003; see discussion in section 1c).

To further examine these waves and their horizontal structure, ERA5 700-hPa geopotential height and wind vector data were collected within 10° of the *TGT* and composited by easterly wave phase (Fig. 17). Also plotted is the precipitation frequency derived from IMERG. Note that the x and y axes of these plots are not absolute geographical coordinates of longitude and latitude, but rather indicate a distance from the ship. The general structure of the geopotential height lines and wind barbs follows what one would expect to see in easterly waves, which have ''inverted trough'' structures (Frank 1969). The ridge phase (Fig. 17a) shows some evidence of a southwest-to-northeast tilt with increasing latitude; however, this tilt is less clear in the other phases. It is apparent in Fig. 17c that the trough phase features the highest probability of precipitation. In the northerly (southerly) panel, the trough of the wave lies to the east (west) of the ship, and is collocated with a region of enhanced precipitation. In the trough panel, much of the map is covered in higher precipitation probabilities. This agrees with the results of Fig. 16, which showed higher relative humidity anomalies associated with troughs.

Looking at precipitation features again, Fig. 18 shows the number of precipitation features as a function of convective morphology and the easterly wave phase within which they occurred. Some patterns are evident, but the unequal sampling

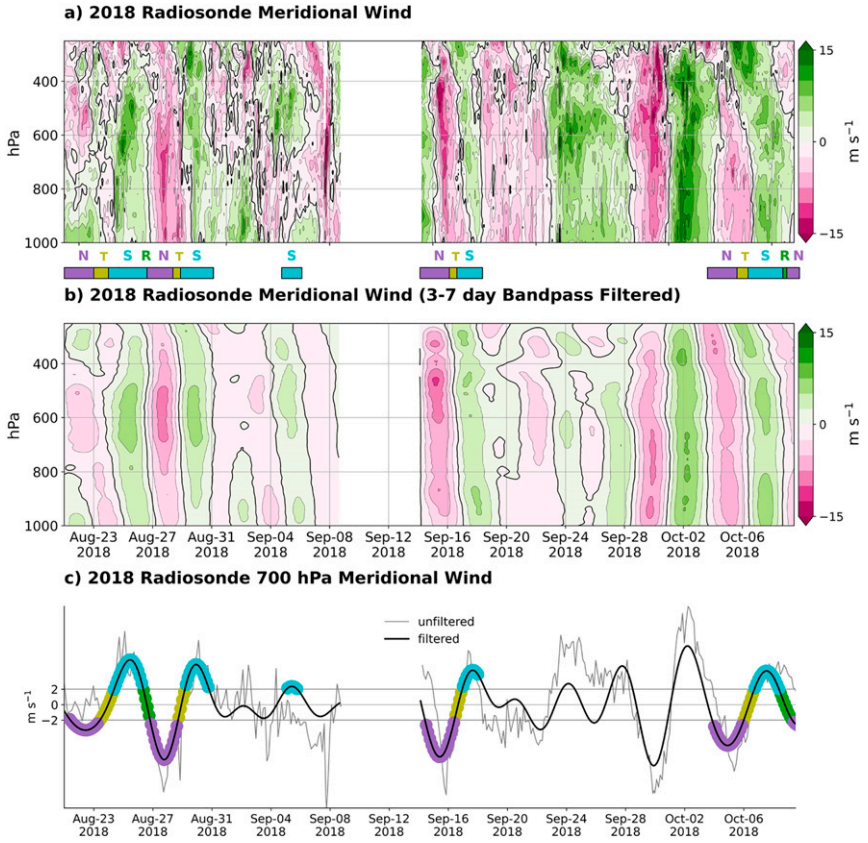

FIG. 15. (a) Meridional wind from PISTON 2018 sounding data, and (b) as in (a), but with a 3–7-day bandpass filter applied. Lines/labels between (a) and (b) indicate whether that period is identified as a northerly (N; purple), trough (T; yellow), southerly (S; cyan), or ridge (R; green) wave phase. (c) Time series of the 700-hPa meridional wind, both with and without the 3–7-day bandpass filter. The wind thresholds for easterly wave detection (-2 and $2\,\mathrm{m\,s^{-1}}$; see section 2d) are marked, and the line is colored by the detected wave phase.

of wave phases during the cruise requires cautious interpretation of this table. For example, although the highest number of isolated features occurred in southerly phases, this is at least in part due to the fact that southerly phases were simply sampled more often than the other phases. On the other hand, even though only slightly more linear MCSs occurred during troughs than during northerly or southerly phases, troughs were sampled much less frequently than northerly or southerly phases, so the high number of linear MCSs is more significant in this regard.

The issue of unequal sampling can be overcome with a random-sampling method, similar to what was described in section 3c. Each radar scan was first labeled by the wave phase it occurred in. Again, 1000 scans were randomly sampled (with replacement) for each of the four phases. Precipitation features were then identified and classified from the resulting 4000 scans, which had an equal number of samples from each wave phase. Figure 19 shows the distribution of wave phases that different feature morphologies occurred under, based on this resampled SEA-POL data. Compared to other feature types, isolated features were most likely to occur during ridge phases. As mentioned previously, ridges were typically associated with reduced relative humidity anomalies throughout the column. These relatively dry conditions were apparently enough to suppress the formation of even moderate-sized sub-MCSs (and certainly MCSs). On the other hand, clearer skies may have led to increased solar insolation and SST increases, which promote the formation of the isolated cells. These shallow cells may be important in moistening the lower troposphere to support more widespread convection later, similar to the ''discharge–recharge'' theory for Madden–Julian oscillation onset (Bladé and Hartmann 1993; Xu and Rutledge 2016).

On the other end of the size and organization spectrum, linear MCSs were by far most likely to occur in the troughs of easterly waves. The high moisture content seen during troughs apparently led to conditions which were conducive for large organized MCSs. The MCSs themselves may also be contributing to the high moisture content seen in Fig. 16. Furthermore, these MCSs also produced broad regions of stratiform rain, which leads to a top-heavy heating profile (Houze 1989; Schumacher et al. 2007; Tao et al. 2010). This is consistent with Fig. 16c, which shows more heating aloft in the trough phase.

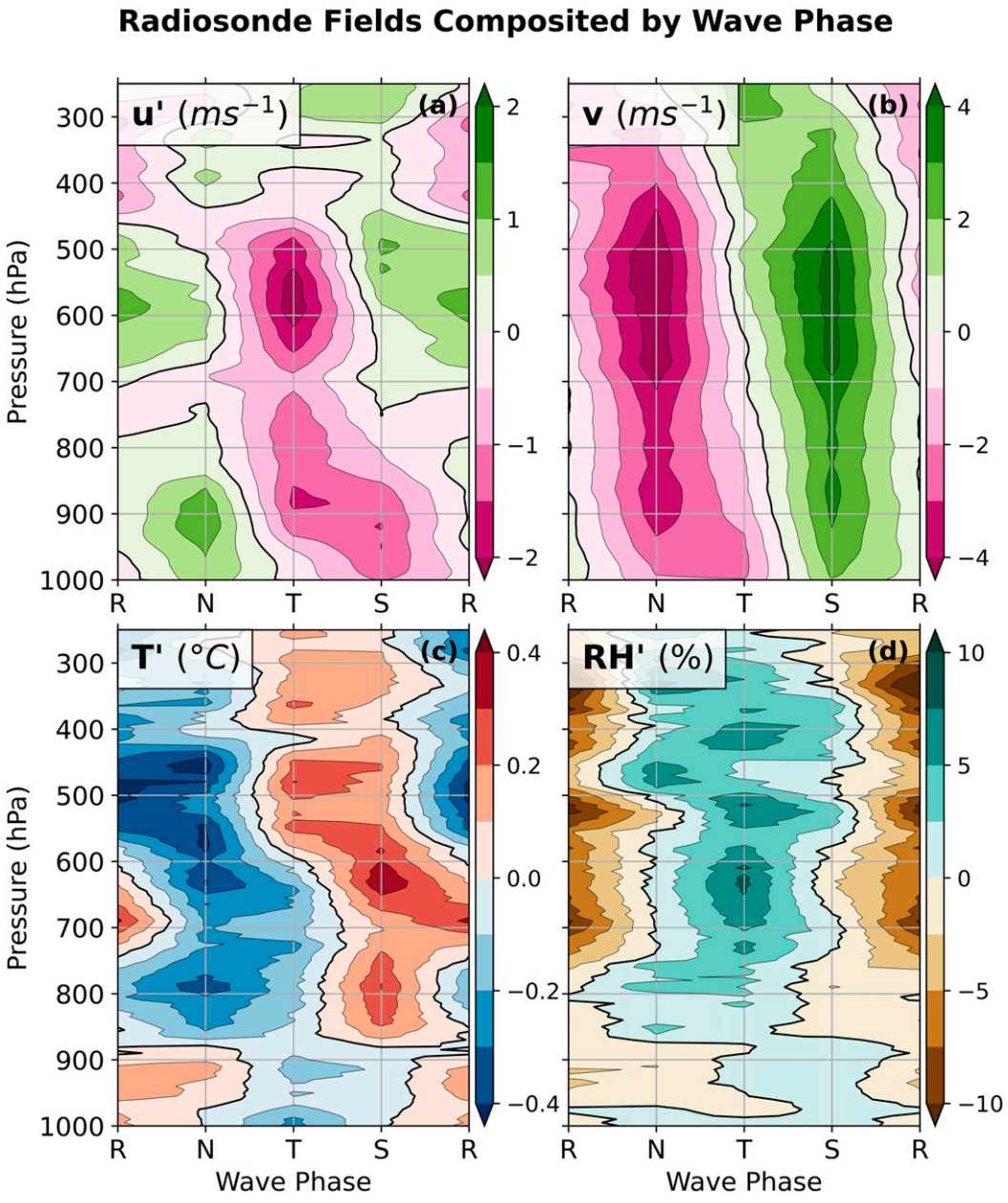

FIG. 16. PISTON 2018 (a) radiosonde zonal wind anomaly, (b) meridional wind, (c) temperature anomaly, and (d) relative humidity anomaly composited by the easterly wave phase in which they occurred (R = ridge, N = northerly, T = trough, S = southerly). Anomalies were calculated against the mean of that variable across the 2018 operations period.

There is also some evidence of deep vertical shear in the meridional wind plot of Fig. 16, which may have acted to expand stratiform regions through detrainment of ice hydrometeors from deep convection (Houze 2004; Yamada et al. 2010). While linear MCSs occurred most often in troughs, nonlinear MCSs were relatively more likely to be associated with southerly phases. As southerly phases follow trough passages, it seems plausible that this transition from linear to nonlinear could be a result of the main convective line of MCSs weakening or moving out of range of SEA-POL as the trough axes passed. On the other hand, sub-MCSs were more likely to be found in northerly phases than MCSs. Northerly phases follow ridges (which featured a relatively high number of isolated features) and precede troughs (which featured a large number of MCSs), so there is evidence that the northerly phases are a sort of "transition zone" from small isolated features to large MCSs. This transition from sub-MCSs (which typically have a relatively high convective fraction) to nonlinear MCSs (which have a high

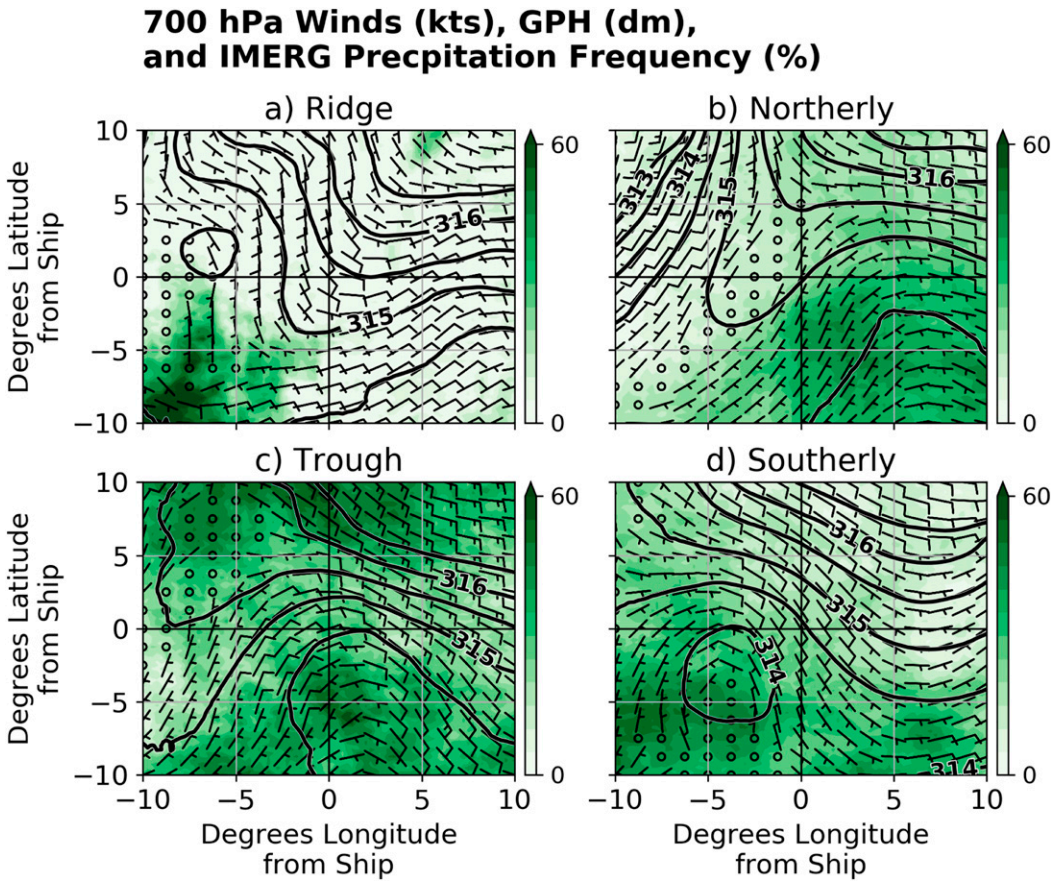

FIG. 17. ERA5 700-hPa wind (barbs), geopotential height (black contours), and IMERG precipitation frequency (green shading) composited by easterly wave phase.

stratiform fraction) as the wave transitions from northerly to trough to southerly agrees with the findings of P03, who noted a transition from convective to stratiform rainfall across the trough axes.

4. Summary and conclusions

During the PISTON field campaign, the CSU SEA-POL radar-sampled convection across a broad spectrum of sizes and organizations. Although no discernable BSISO event occurred, the ships encountered a wide variety of other interesting large-scale atmospheric phenomena, such as easterly waves and typhoons. The purpose of this study was to analyze the convection observed by SEA-POL during PISTON, and to tie the variability in convective morphology to the large-scale conditions the convection was embedded within.

During the 2018 cruise (particularly in the first half), much of the variability was characterized by the passage of easterly waves on 3–5-day time scales. The 2018 cruise was also marked by the passage of several tropical cyclones, the outer rainbands of which impacted the ship as the storms moved to the north. Several of these storms also produced ''monsoon tails,'' wherein a belt of southwesterly winds and enhanced precipitation connected the core of the monsoon region over the South China Sea and Bay of Bengal to the southern flank inflow of the cyclones. These monsoon tails and associated rainfall tended to persist in the operations area even after the tropical system had moved well away from the ship. The largest precipitation events during 2018 were generally tied to the passage of these typhoons.

While 2018 featured numerous easterly waves and typhoons all impacting the ship separately, the weather on the 2019 cruise was mainly controlled by one phenomenon: a large monsoon gyre that meandered about the western North Pacific for most of the operational period. Designated as Invest 95W by the JTWC, the broad cyclonic system fluctuated in intensity and organization for much of the cruise, before eventually becoming Tropical Storm Tapah. Variation in wind profiles at the ship was mainly tied to the location of 95W/Tapah, and variation in precipitation tied to fluctuations in the monsoon gyre's organization.

An automated precipitation feature detection/classification algorithm (which was updated from the XR15 method to more accurately distinguish linear convective feature) was run on both years of the SEA-POL dataset. It was found that occurrence frequency and rain volume contribution had an opposite relation the feature size. That is, smaller features occurred more frequently but produced less of the total rain, while larger

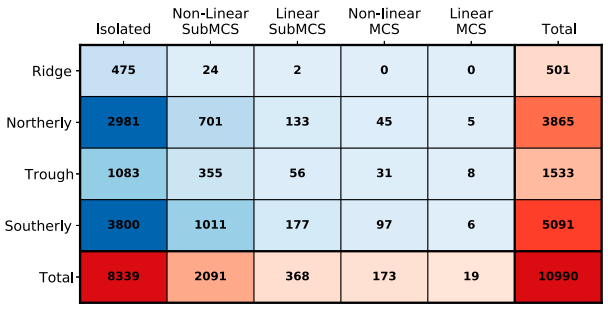

FIG. 18. PISTON 2018 precipitation feature count by wave phase and morphology. Darker colors correspond to higher numbers, with the "total" boxes being colored on a separate scale.

features occurred infrequently but produced a disproportionate fraction of the rain. For example, isolated features (<20 km in length) were present in 91% of radar scans, and contributed 11% of the total rain volume. Conversely, MCSs (area > 2000 km^2) were present in only 13% of scans yet were responsible for 56% of the total rain volume. Larger features also tended to be more intense, as defined by larger mean convective rain rates and taller 30-dBZ echo-top heights. It is hypothesized that this is a result of convection in larger features being shielded from entrainment of dry air. Linear features also tended to be more intense than their nonlinear counterparts, possibly due to the impact of vorticity balance between cold pools and wind shear (Rotunno et al. 1988; Weisman et al. 1988; Weisman and Rotunno 2004).

Precipitation feature statistics were examined as a function of the environmental conditions in which they occurred. It was found that southwesterly wind regimes brought a higher likelihood of MCSs, while nonsouthwesterly regimes featured all morphologies at approximately equal frequencies. The finding of more MCSs in southwesterly wind regimes, which can be thought of as periods with an active monsoon flow, agrees with the results of Xu and Rutledge (2018) and Chudler et al. (2020), which linked the increase in feature size to an increase in wind shear and midtropospheric moisture. Similarly, MCSs were also found to preferentially form when low-level wind shear was greatest. Conversely, CAPE and SSTs were found to be lower when MCSs were present. This may be a result of the MCSs themselves impacting the environment in ways that reduce CAPE and SSTs. Linear sub-MCSs were found to occur in higher low-level wind shear than nonlinear sub-MCSs, agreeing with previous studies suggesting that low-level wind shear is important in generating organized convective lines (Houze and Cheng 1997; Rotunno et al. 1988; LeMone 1998; Weisman et al. 1988; Weisman and Rotunno 2004; Liu and Zipser 2013).

Finally, the environmental conditions associated with the different phases of easterly waves were examined, as well as the precipitation features that occurred in them. Before summarizing these results, it is important to note that only a small sample of waves (two full waves and two partial waves) were observed during PISTON. Therefore our results are likely not necessarily representative of all easterly waves in the region, and caution should be exercised in making any general conclusions. That being said, to our knowledge there have been no

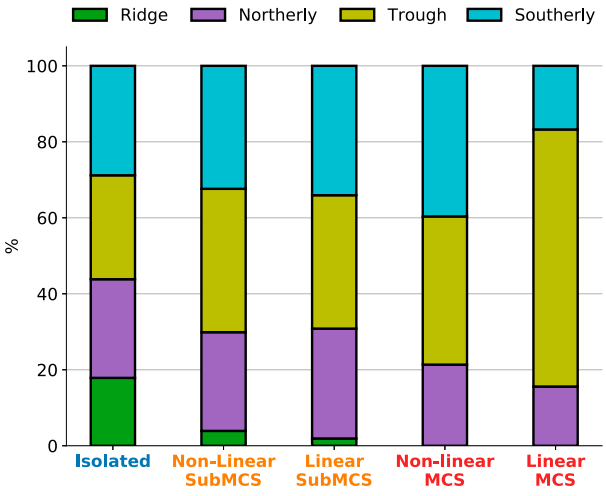

FIG. 19. Distribution of the easterly wave phases under which different precipitation feature morphologies occurred.

in situ field campaign measurements of easterly waves in the northern west Pacific, so the results are still valuable and could serve as a focus of further research.

Vertical profiles of u and v were found to be 90° out of phase, in contrast with previous studies that showed positive correlation between the two. This has important implications for barotropic conversion and energy extraction from the mean flow, thought to be a main source of energy for easterly waves in this region. Because positive precipitation anomalies were correlated with positive temperature anomalies, it is possible that the easterly waves observed during PISTON relied on diabatic heating as a main source of energy. One explanation for the apparent lack of barotropic processes is that these waves were observed farther east than the region where maximum strengthening usually occurs, so perhaps baroclinic conversion processes had not yet begun. It was also found that the troughs (ridges) of waves were associated with moist (dry) relative humidity anomalies, also in slight contradiction to previous analysis. With regard to precipitation features, ridges featured a relatively high number of isolated features and troughs a high number of linear MCSs; northerly and southerly phases were found to act as a transition zone between the two.

Several other areas of future research exist for the PISTON dataset. While this study focused on large-scale conditions and statistics of precipitation features, future studies will examine individual convective events on a case study basis, using the SEA-POL polarimetric data and detailed vertical cross-section scans. The polarimetric data in particular will provide important insights into the microphysical characteristics of convection in the western Pacific, and analysis on this topic is already underway. The impact of rainfall on the ocean surface (and vice versa) using a freshwater lens detection algorithm such as in Thompson et al. (2019) is also an enticing avenue for future work. Although this study primarily examined convection within the 120-km range of SEA-POL, it also lays the foundation for future work looking at the impact of this convection on the global climate system. For example, because this

study links convective morphologies to environmental conditions and synoptic patterns, analysis on the frequency at which these conditions and patterns occur would lead to insights on the broader-scale impacts of this convection on the atmosphere. Overall, the suite of scientific instrumentation on board the *TGT* and *SR* captured a multitude of atmospheric and oceanic measurements, and the multifaceted dataset affords exciting opportunities to comprehensively examine the weather phenomena which were observed.

Acknowledgments. This research was funded by the Office of Naval Research Grant N00014-16-1-3092. Thanks to Chris Fairall, Elizabeth Thompson, Sergio Pezoa (NOAA PSL), Ludovic Bariteau, Byron Blomquist (CU CIRES), and Simon de Szoke (OSU) for processing and access to the air–sea flux dataset (used for SST). Thanks to Prof. Eric Maloney at Colorado State University for his input on the easterly wave analysis. Thanks to Brenda Dolan and Paul Ciesielski at Colorado State University for their work on quality control of the SEA-POL and sounding datasets, respectively. Special thanks to the crews of the *R/V Thomas G. Thompson* and *R/V Sally Ride* for allowing and assisting with the setup of SEA-POL on these ships.

Data availability statement. Data from the PISTON field campaign, including the sounding and SEA-POL radar datasets used in this research, are available to download at https://www-air.larc.nasa.gov/cgi-bin/ArcView/camp2ex. IMERG satellite data can be downloaded from NASA Goddard Earth Sciences Data and Information Services Center (https://disc.gsfc.nasa.gov/datasets/GPM_3IMERGHH_06/summary). ERA5 datasets can be accessed at https://www.ecmwf.int/en/forecasts/datasets/reanalysis-datasets/era5. IBTrACS data can be accessed at https://www.ncdc.noaa.gov/ibtracs/.

REFERENCES

Avila, L. A., and R. J. Pasch, 1992: Atlantic tropical systems of 1991. *Mon. Wea. Rev.*, **120**, 2688–2696, https://doi.org/10.1175/1520-0493(1992)120<2688:ATSO>2.0.CO;2.

Beattie, J. C., and R. L. Elsberry, 2012: Western North Pacific monsoon depression formation. *Wea. Forecasting*, **27**, 1413–1432, https://doi.org/10.1175/WAF-D-11-00094.1.

Bladé, I., and D. L. Hartmann, 1993: Tropical intraseasonal oscillations in a simple nonlinear model. *J. Atmos. Sci.*, **50**, 2922–2939, https://doi.org/10.1175/1520-0469(1993)050<2922:TIOIAS>2.0.CO;2.

Burpee, R. W., 1972: The origin and structure of easterly waves in the lower troposphere of North Africa. *J. Atmos. Sci.*, **29**, 77–90, https://doi.org/10.1175/1520-0469(1972)029<0077:TOASOE>2.0.CO;2.

——, 1974: Characteristics of North African easterly waves during the summers of 1968 and 1969. *J. Atmos. Sci.*, **31**, 1556–1570, https://doi.org/10.1175/1520-0469(1974)031<1556:CONAEW>2.0.CO;2.

——, 1975: Some features of synoptic-scale waves based on a compositing analysis of GATE data. *Mon. Wea. Rev.*, **103**, 921–925, https://doi.org/10.1175/1520-0493(1975)103<0921:SFOSWB>2.0.CO;2.

Chang, C., 1970: Westward propagating cloud patterns in the tropical Pacific as seen from time-composite satellite photographs. *J. Atmos. Sci.*, **27**, 133–138, https://doi.org/10.1175/1520-0469(1970)027<0133:WPCPIT>2.0.CO;2.

Chudler, K., W. Xu, and S. A. Rutledge, 2020: Impact of the boreal summer intraseasonal oscillation on the diurnal cycle of precipitation near and over the island of Luzon. *Mon. Wea. Rev.*, **148**, 1805–1827, https://doi.org/10.1175/MWR-D-19-0252.1.

Ciesielski, P. E., and Coauthors, 2014: Quality-controlled upper-air sounding dataset for DYNAMO/CINDY/AMIE: Development and corrections. *J. Atmos. Oceanic Technol.*, **31**, 741–764, https://doi.org/10.1175/JTECH-D-13-00165.1.

Cifelli, R., and S. A. Rutledge, 1998: Vertical motion, diabatic heating, and rainfall characteristics in north Australia convective systems. *Quart. J. Roy. Meteor. Soc.*, **124**, 1133–1162, https://doi.org/10.1002/qj.49712454806.

Dickinson, M., and J. Molinari, 2002: Mixed Rossby–gravity waves and western Pacific tropical cyclogenesis. Part I: Synoptic evolution. *J. Atmos. Sci.*, **59**, 2183–2196, https://doi.org/10.1175/1520-0469(2002)059<2183:MRGWAW>2.0.CO;2.

Donner, L. J., C. J. Seman, and R. S. Hemler, 1999: Three-dimensional cloud-system modeling of GATE convection. *J. Atmos. Sci.*, **56**, 1885–1912, https://doi.org/10.1175/1520-0469(1999)056<1885:TDCSMO>2.0.CO;2.

Dunkerton, T. J., M. Montgomery, and Z. Wang, 2009: Tropical cyclogenesis in a tropical wave critical layer: Easterly waves. *Atmos. Chem. Phys.*, **9**, 5587–5646, https://doi.org/10.5194/acp-9-5587-2009.

Edson, J. B., and Coauthors, 2013: On the exchange of momentum over the open ocean. *J. Phys. Oceanogr.*, **43**, 1589–1610, https://doi.org/10.1175/JPO-D-12-0173.1.

Frank, N. L., 1969: The ''inverted V'' cloud pattern—An easterly wave? *Mon. Wea. Rev.*, **97**, 130–140, https://doi.org/10.1175/1520-0493(1969)097<0130:TVCPEW>2.3.CO;2.

Godfrey, J. S., R. A. Houze Jr., R. H. Johnson, R. Lukas, J.-L. Redelsperger, A. Sumi, and R. Weller, 1998: Coupled Ocean–Atmosphere Response Experiment (COARE): An interim report. *J. Geophys. Res.*, **103**, 14395–14450, https://doi.org/10.1029/97JC03120.

Hartmann, D. L., H. H. Hendon, and R. A. Houze Jr., 1984: Some implications of the mesoscale circulations in tropical cloud clusters for large-scale dynamics and climate. *J. Atmos. Sci.*, **41**, 113–121, https://doi.org/10.1175/1520-0469(1984)041<0113:SIOTMC>2.0.CO;2.

Hersbach, H., and Coauthors, 2020: The ERA5 global reanalysis. *Quart. J. Roy. Meteor. Soc.*, **146**, 1999–2049, https://doi.org/10.1002/qj.3803.

Houze, R. A., Jr., 1989: Observed structure of mesoscale convective systems and implications for large-scale heating. *Quart. J. Roy. Meteor. Soc.*, **115**, 425–461, https://doi.org/10.1002/qj.49711548702.

——, 1997: Stratiform precipitation in regions of convection: A meteorological paradox? *Bull. Amer. Meteor. Soc.*, **78**, 2179–2196, https://doi.org/10.1175/1520-0477(1997)078<2179:SPIROC>2.0.CO;2.

——, 2004: Mesoscale convective systems. *Rev. Geophys.*, **42**, RG4003, https://doi.org/10.1029/2004RG000150.

——, 2014: *Cloud Dynamics*. Academic Press, 432 pp.

——, and C. Cheng, 1977: Radar characteristics of tropical convection observed during GATE: Mean properties and trends over the summer season. *Mon. Wea. Rev.*, **105**, 964–980, https://doi.org/10.1175/1520-0493(1977)105<0964:RCOTCO>2.0.CO;2.

Kiladis, G. N., C. D. Thorncroft, and N. M. J. Hall, 2006: Three-dimensional structure and dynamics of African easterly waves.

Part I: Observations. *J. Atmos. Sci.*, **63**, 2212–2230, https://doi.org/10.1175/JAS3741.1.

Knapp, K. R., M. C. Kruk, D. H. Levinson, H. J. Diamond, and C. J. Neumann, 2010: The International Best Track Archive for Climate Stewardship (IBTrACS): Unifying tropical cyclone data. *Bull. Amer. Meteor. Soc.*, **91**, 363–376, https://doi.org/10.1175/2009BAMS2755.1.

——, H. J. Diamond, J. P. Kossin, M. C. Kruk, C. J. Schreck, 2018: International Best Track Archive for Climate Stewardship (IBTrACS) Project, version 4. NOAA National Centers for Environmental Information, accessed 11 June 2020, https://doi.org/10.25921/82ty-9e16.

Lang, T. J., D. A. Ahijevych, S. W. Nesbitt, R. E. Carbone, S. A. Rutledge, and R. Cifelli, 2007: Radar-observed characteristics of precipitating systems during NAME 2004. *J. Climate*, **20**, 1713–1733, https://doi.org/10.1175/JCLI4082.1.

Lau, K.-H., and N.-C. Lau, 1990: Observed structure and propagation characteristics of tropical summertime synoptic scale disturbances. *Mon. Wea. Rev.*, **118**, 1888–1913, https://doi.org/10.1175/1520-0493(1990)118<1888:OSAPCO>2.0.CO;2.

——, and ——, 1992: The energetics and propagation dynamics of tropical summertime synoptic-scale disturbances. *Mon. Wea. Rev.*, **120**, 2523–2539, https://doi.org/10.1175/1520-0493(1992)120<2523:TEAPDO>2.0.CO;2.

Lee, J., B. Wang, M. C. Wheeler, X. Fu, D. E. Waliser, and I. Kang, 2013: Real-time multivariate indices for the boreal summer intraseasonal oscillation over the Asian summer monsoon region. *Climate Dyn.*, **40**, 493–509, https://doi.org/10.1007/s00382-012-1544-4.

Lee, S., J. Moon, B. Wang, and H. Kim, 2017: Subseasonal prediction of extreme precipitation over Asia: Boreal summer intraseasonal oscillation perspective. *J. Climate*, **30**, 2849–2865, https://doi.org/10.1175/JCLI-D-16-0206.1.

LeMone, M. A., 1983: Momentum transport by a line of cumulonimbus. *J. Atmos. Sci.*, **40**, 1815–1834, https://doi.org/10.1175/1520-0469(1983)040<1815:MTBALO>2.0.CO;2.

——, G. M. Barnes, and E. J. Zipser, 1984: Momentum flux by lines of cumulonimbus over the tropical oceans. *J. Atmos. Sci.*, **41**, 1914–1932, https://doi.org/10.1175/1520-0469(1984)041<1914:MFBLOC>2.0.CO;2.

——, E. J. Zipser, and S. B. Trier, 1998: The role of environmental shear and thermodynamic conditions in determining the structure and evolution of mesoscale convective systems during TOGA COARE. *J. Atmos. Sci.*, **55**, 3493–3518, https://doi.org/10.1175/1520-0469(1998)055<3493:TROESA>2.0.CO;2.

Liu, C., and E. Zipser, 2013: Regional variation of morphology of organized convection in the tropics and subtropics. *J. Geophys. Res.*, **118**, 453–466, https://doi.org/10.1029/2012JD018409.

Maloney, E. D., and M. J. Dickinson, 2003: The intraseasonal oscillation and the energetics of summertime tropical western North Pacific synoptic-scale disturbances. *J. Atmos. Sci.*, **60**, 2153–2168, https://doi.org/10.1175/1520-0469(2003)060<2153:TIOATE>2.0.CO;2.

Medioni, G., M. Lee, and C. Tang, 2000: *A Computational Framework for Segmentation and Grouping*. Elsevier, 284 pp.

Molinari, J., D. Knight, M. Dickinson, D. Vollaro, and S. Skubis, 1997: Potential vorticity, easterly waves, and eastern Pacific tropical cyclogenesis. *Mon. Wea. Rev.*, **125**, 2699–2708, https://doi.org/10.1175/1520-0493(1997)125<2699:PVEWAE>2.0.CO;2.

Moon, J., B. Wang, K. Ha, and J. Lee, 2013: Teleconnections associated with Northern Hemisphere summer monsoon intraseasonal oscillation. *Climate Dyn.*, **40**, 2761–2774, https://doi.org/10.1007/s00382-012-1394-0.

Nesbitt, S. W., R. Cifelli, and S. A. Rutledge, 2006: Storm morphology and rainfall characteristics of TRMM precipitation features. *Mon. Wea. Rev.*, **134**, 2702–2721, https://doi.org/10.1175/MWR3200.1.

Petersen, W. A., R. Cifelli, D. J. Boccippio, S. A. Rutledge, and C. Fairall, 2003: Convection and easterly wave structures observed in the eastern Pacific warm pool during EPIC-2001. *J. Atmos. Sci.*, **60**, 1754–1773, https://doi.org/10.1175/1520-0469(2003)060<1754:CAEWSO>2.0.CO;2.

Ramsay, H., 2017: *The Global Climatology of Tropical Cyclones*, Oxford Research Encyclopedia of Natural Hazard Science, https://doi.org/10.1093/acrefore/9780199389407.013.79.

Reed, R. J., and E. E. Recker, 1971: Structure and properties of synoptic-scale wave disturbances in the equatorial western Pacific. *J. Atmos. Sci.*, **28**, 1117–1133, https://doi.org/10.1175/1520-0469(1971)028<1117:SAPOSS>2.0.CO;2.

Rickenbach, T. M., and S. A. Rutledge, 1998: Convection in TOGA COARE: Horizontal scale, morphology, and rainfall production. *J. Atmos. Sci.*, **55**, 2715–2729, https://doi.org/10.1175/1520-0469(1998)055<2715:CITCHS>2.0.CO;2.

Rotunno, R., J. B. Klemp, and M. L. Weisman, 1988: A theory for strong, long-lived squall lines. *J. Atmos. Sci.*, **45**, 463–485, https://doi.org/10.1175/1520-0469(1988)045<0463:ATFSLL>2.0.CO;2.

Rutledge, S. A., V. Chandrasekar, B. Fuchs, J. George, F. Junyent, P. Kennedy, and B. Dolan, 2019a: Deployment of the SEA-POL C-band polarimetric radar to SPURS-2. *Oceanography*, **32**, 50–57, https://doi.org/10.5670/oceanog.2019.212.

——, ——, ——, ——, ——, B. Dolan, P. C. Kennedy, and K. Drushka, 2019b: SEA-POL goes to sea. *Bull. Amer. Meteor. Soc.*, **100**, 2285–2301, https://doi.org/10.1175/BAMS-D-18-0233.1.

Schumacher, C., and R. A. Houze, 2003: The TRMM Precipitation Radar's view of shallow, isolated rain. *J. Appl. Meteor.*, **42**, 1519–1524, https://doi.org/10.1175/1520-0450(2003)042<1519:TTPRVO>2.0.CO;2.

——, M. H. Zhang, and P. E. Ciesielski, 2007: Heating structures of the TRMM field campaigns. *J. Atmos. Sci.*, **64**, 2593–2610, https://doi.org/10.1175/JAS3938.1.

Serra, Y. L., G. N. Kiladis, and M. F. Cronin, 2008: Horizontal and vertical structure of easterly waves in the Pacific ITCZ. *J. Atmos. Sci.*, **65**, 1266–1284, https://doi.org/10.1175/2007JAS2341.1.

Sobel, A. H., S. E. Yuter, C. S. Bretherton, and G. N. Kiladis, 2004: Large-scale meteorology and deep convection during TRMM KWAJEX. *Mon. Wea. Rev.*, **132**, 422–444, https://doi.org/10.1175/1520-0493(2004)132<0422:LMADCD>2.0.CO;2.

——, J. Sprintall, E. D. Maloney, Z. K. Martin, S. Wang, S. deSzoeke, B. Trabing, and S. A. Rutledge, 2020: Large-scale state and evolution of the atmosphere and ocean during PISTON 2018. *J. Climate*, **34**, 5017–5035, https://doi.org/10.1175/JCLI-D-20-0517.1.

Steiner, M., R. A. Houze Jr., and S. E. Yuter, 1995: Climatological characterization of three-dimensional storm structure from operational radar and rain gauge data. *J. Appl. Meteor.*, **34**, 1978–2007, https://doi.org/10.1175/1520-0450(1995)034<1978:CCOTDS>2.0.CO;2.

Tan, J., G. J. Huffman, D. T. Bolvin, and E. J. Nelkin, 2019: IMERG V06: Changes to the morphing algorithm. *J. Atmos. Oceanic Technol.*, **36**, 2471–2482, https://doi.org/10.1175/JTECH-D-19-0114.1.

Tao, W., S. Lang, X. Zeng, S. Shige, and Y. Takayabu, 2010: Relating convective and stratiform rain to latent heating. *J. Climate*, **23**, 1874–1893, https://doi.org/10.1175/2009JCLI3278.1.

Thompson, E. J., S. A. Rutledge, B. Dolan, M. Thurai, and V. Chandrasekar, 2018: Dual-polarization radar rainfall estimation over tropical oceans. *J. Appl. Meteor. Climatol.*, **57**, 755–775, https://doi.org/10.1175/JAMC-D-17-0160.1.

——, J. N. Moum, C. W. Fairall, and S. A. Rutledge, 2019: Wind limits on rain layers and diurnal warm layers. *J. Geophys. Res. Oceans*, **124**, 897–924, https://doi.org/10.1029/2018JC014130.

Thompson, R. M., S. W. Payne, E. E. Recker, and R. J. Reed, 1979: Structure and properties of synoptic-scale wave disturbances in the intertropical convergence zone of the eastern Atlantic. *J. Atmos. Sci.*, **36**, 53–72, https://doi.org/10.1175/1520-0469(1979)036<0053:SAPOSS>2.0.CO;2.

Thorncroft, C. D., and B. J. Hoskins, 1994a: An idealized study of African easterly waves. I: A linear view. *Quart. J. Roy. Meteor. Soc.*, **120**, 953–982, https://doi.org/10.1002/qj.49712051809.

——, and ——, 1994b: An idealized study of African easterly waves. II: A nonlinear view. *Quart. J. Roy. Meteor. Soc.*, **120**, 983–1015, https://doi.org/10.1002/qj.49712051810.

Thorpe, A., M. Miller, and M. Moncrieff, 1982: Two-dimensional convection in non-constant shear: A model of mid-latitude squall lines. *Quart. J. Roy. Meteor. Soc.*, **108**, 739–762, https://doi.org/10.1002/qj.49710845802.

Wang, B., and X. Xie, 1997: A model for the boreal summer intraseasonal oscillation. *J. Atmos. Sci.*, **54**, 72–86, https://doi.org/10.1175/1520-0469(1997)054<0072:AMFTBS>2.0.CO;2.

Wang, X., and M. Zhang, 2015: The coupling of mixed Rossby-gravity waves with diabatic heating during the TRMM-KWAJEX field campaign. *Geophys. Res. Lett.*, **42**, 8241–8249, https://doi.org/10.1002/2015GL065813.

Wang, Y., and V. Chandrasekar, 2009: Algorithm for estimation of the specific differential phase. *J. Atmos. Oceanic Technol.*, **26**, 2565–2578, https://doi.org/10.1175/2009JTECHA1358.1.

Weisman, M. L., and R. Rotunno, 2004: "A theory for strong long-lived squall lines" revisited. *J. Atmos. Sci.*, **61**, 361–382, https://doi.org/10.1175/1520-0469(2004)061<0361:ATFSLS>2.0.CO;2.

——, J. B. Klemp, and R. Rotunno, 1988: Structure and evolution of numerically simulated squall lines. *J. Atmos. Sci.*, **45**, 1990–2013, https://doi.org/10.1175/1520-0469(1988)045<1990:SAEONS>2.0.CO;2.

Whitaker, J. W., and E. D. Maloney, 2020: Genesis of an East Pacific easterly wave from a Panama Bight MCS: A case study analysis from June 2012. *J. Atmos. Sci.*, **77**, 3567–3584, https://doi.org/10.1175/JAS-D-20-0032.1.

Xu, W., and S. A. Rutledge, 2015: Morphology, intensity, and rainfall production of MJO convection: Observations from DYNAMO shipborne radar and TRMM. *J. Atmos. Sci.*, **72**, 623–640, https://doi.org/10.1175/JAS-D-14-0130.1.

——, and ——, 2016: Time scales of shallow-to-deep convective transition associated with the onset of Madden–Julian oscillations. *Geophys. Res. Lett.*, **43**, 2880–2888, https://doi.org/10.1002/2016GL068269.

——, and ——, 2018: Convective variability associated with the boreal summer intraseasonal oscillation in the South China Sea region. *J. Climate*, **31**, 7363–7383, https://doi.org/10.1175/JCLI-D-18-0091.1.

Yamada, H., K. Yoneyama, M. Katsumata, and R. Shirooka, 2010: Observations of a super cloud cluster accompanied by synoptic-scale eastward-propagating precipitating systems over the Indian Ocean. *J. Atmos. Sci.*, **67**, 1456–1473, https://doi.org/10.1175/2009JAS3151.1.